ADVANCED FUNCTIONAL MATERIALS
www.afm-journal.de

# Eco-Fabricated Nanowave-Textured Implants Drive Microtubule-Assisted Nuclear Mechanotransduction and Chromatin Modification: Biophysical Priming for Osteogenesis and Bone Regeneration

*Bosu Jeong, Ji-Young Yoon, Junyong Ahn, Byunghak Lee, Sung-Min Park, Jae-Heon Kim, Buuvee Bayarkhangai, Yu Jin Kim, Sak Lee, Jonathan C. Knowles, Moon-Young Kim, DongJun Lee, Sang-Hoon Rhee,* Hae-Hyoung Lee,* Hae-Won Kim,* and Jung-Hwan Lee**

**The biophysical cues from implantable materials, specifically nanotopography, play a pivotal role in directing cellular lineage specification, thereby accelerating tissue healing and regeneration. Despite the recognized impact of these cues, the mechanisms governing mechano-activated signaling pathways between the cytoskeletal and nuclear domains remain largely unexplored. Here, the processes underlying the enhanced osteogenesis of mesenchymal stem cells (MSCs) driven by nanotextured implants are elucidated, focusing on alterations in cytoskeletal mechanosensitive molecules and nuclear chromatin structures. Using green-processed femtosecond laser fabrication, an implant platform featuring nanowave textures is engineered, inducing cellular alignment with oriented cytoskeletons and consequential changes in nuclear shape. Notably, activated and aligned microtubules alongside the nucleus play a key role in shaping nuclear morphology. The nanowave textures induce significant modifications in chromatin structure, characterized by increased histone acetylation, implying a mechano-priming of MSCs for osteogenesis. Mechanically-primed MSCs exhibit enhanced osteogenic transcriptional responsiveness to biochemical cues, with mechanosensitive YAP co-signaling with the RUNX2, facilitated by an opened chromatin structure. In vivo experiments in a rabbit tibia reveal that nanowave-textured implants promote osteogenesis and bone formation. This study underscores the ability of nanowave-textured cues to transmit mechano-signals across the cytoskeletal-to-nuclear space in MSCs, leading to stimulated osteogenesis.**

## 1. Introduction

Controlled nanostructures on implantable materials have emerged as powerful modulators of cellular behavior, particularly in directing stem cell fate and tissue regeneration. The interaction between nanotopographical features and cellular components - from the plasma membrane to the nucleus - represents a crucial interface for controlling cellular mechanotransduction.[1] While conventional surface modification approaches have demonstrated the importance of topographical cues, the precise mechanisms by which these physical signals are transmitted from the cell surface to the nucleus, ultimately influencing cell fate decisions, remain incompletely understood.[2] Particularly intriguing is the role of cytoskeletal elements, especially microtubules, in translating nanotopographical cues into nuclear and chromatin modifications that drive osteogenic differentiation.[3]

Medical and dental implants, bone plates, screws, pins, and bone graft substitutes face increasing demand in our

B. Jeong, S.-H. Rhee
Department of Dental Biomaterials Science
Dental Research Institute
School of Dentistry
Seoul National University
Seoul 03080, Republic of Korea
E-mail: rhee1213@snu.ac.kr

The ORCID identification number(s) for the author(s) of this article can be found under https://doi.org/10.1002/adfm.202503422



**DOI: 10.1002/adfm.202503422**

B. Jeong, B. Lee
Surface Science Research Center
B2LAB Co.
Ltd
Seoul 05836, Republic of Korea

J.-Y. Yoon, J. Ahn, S.-M. Park, J.-H. Kim, B. Bayarkhangai, Y. J. Kim, D. Lee, H.-H. Lee, H.-W. Kim, J.-H. Lee
Institute of Tissue Regeneration Engineering (ITREN)
Dankook University
Cheonan, Chungcheongnam-do 31116, Republic of Korea
E-mail: haelee@dankook.ac.kr; kimhw@dku.edu; ducious@dankook.ac.kr

aging society, where trauma and disease frequently challenge effective bone regeneration.[4] This has motivated efforts to identify improved biomaterial surface designs through mechanotuning or therapeutic-ingredient immobilization to enhance clinical outcomes.[5] Current clinically available surface modification techniques, such as sandblasting and acid-etching (SLA) for titanium implants, present significant environmental concerns due to hazardous strong acid waste management, costly chemical disposal requirements, and worker safety risks from toxic fume exposure.[6] Moreover, these conventional approaches often fail to fully leverage the potential of nanoscale topography in directing cellular mechanotransduction for enhanced bone formation. While more advanced techniques such as anodizing, block copolymer lithography, and electron-beam lithography can achieve superior sub-100 nm resolution features with precise control, these approaches typically require specialized equipment, complex processing steps with toxic chemicals, and may present scalability challenges for clinical translation.[7]

To address these limitations, we optimized a femtosecond laser (FsL) as a significant advancement over conventional chemical/plasma etching, anodizing, and lithographic approaches (Table S1, Supporting Information). The optimized FsL technique directly modifies titanium surfaces through laser-induced plasma formation and surface plasmon coupling mechanisms, generating controlled sub-wavelength periodic surface nanotextures without additional steps, environmentally harmful ingredients, or causing undesired recast surface formation and debris deposition from thermal damage[8] (Table S2 and Note S1, Supporting Information). This direct patterning approach is able to create consistent aligned nanowaves even on complex 3D implant geometries—a critical advantage for clinical applications. This combination of nanoscale precision, manufacturing efficiency, and environmental sustainability positions FsL fabrication as an ideal approach for next-generation medical implant surfaces designed to enhance osseointegration.

Here, we present an environmentally sustainable approach using FsL fabrication to create wave-formed nanotexture (W-NT) surfaces on various implant materials, including titanium. This green-processed (strong acid-free) technique achieves a remarkable four-fold increase in nano-scale surface roughness while maintaining bulk mechanical integrity, addressing both environmental concerns and performance requirements. Our study reveals a previously unrecognized mechanistic cascade whereby nanowave textures activate microtubule-mediated force transmission, leading to cell elongation, nuclear deformation, and subsequent chromatin remodeling in MSCs. Through comprehensive ATAC-sequencing and RNA-sequencing analyses, we demonstrate that this chromatin loosening, characterized by distinct histone-3 acetylation patterns, enhances cellular responsiveness to osteogenic cues. The mechanistic pathway connecting 'wave-formed nanotexture' – 'microtubule' – 'nuclear deformation' orchestrates the activation of YAP and RUNX2, coupled with histone-3 acetylation, ultimately promoting osteogenesis. The clinical relevance of these findings is validated in rabbit femoral defect models, where W-NT Ti implants significantly enhanced bone regeneration without requiring exogenous factors, outperforming conventional controls over a 4-week period. These results establish eco-friendly fabricated nanotopography as a potent interface for modulating MSC chromatin architecture and optimizing medical device osteointegration.

## 2. Results

### 2.1. A Conceptual Framework for Nanowave-Textured Titanium Implants: From Femtosecond Laser Engineering to Chromatin Priming

Nanotextured surfaces were eco-fabricated on medical-grade titanium (Ti, grade 4) specimens using a custom-built, optimized

J.-Y. Yoon, S.-M. Park, B. Bayarkhangai, J. C. Knowles, H.-H. Lee, H.-W. Kim, J.-H. Lee
Department of Nanobiomedical Science and BK21 PLUS NBM Global Research Center for Regenerative Medicine
Dankook University
Cheonan, Chungcheongnam-do 31116, Republic of Korea
J.-Y. Yoon, J.-H. Lee
Institute for Stem Cell & Matters
Cell & Matter Corporation
Cheonan 31116, Republic of Korea
J. Ahn, J.-H. Kim, Y. J. Kim, H.-H. Lee, H.-W. Kim, J.-H. Lee
Department of Biomaterials Science
College of Dentistry
Dankook University
Cheonan, Chungcheongnam-do 31116, Republic of Korea
S. Lee
Department of Oral Pathology
Seoul National University Dental Hospital
Seoul 03080, Republic of Korea
S. Lee
Department of Oral Pathology
School of Dentistry
Seoul National University
Seoul 03080, Republic of Korea
J. C. Knowles, H.-H. Lee, H.-W. Kim, J.-H. Lee
UCL Eastman-Korea Dental Medicine Innovation Centre
Dankook University
Cheonan, Chungcheongnam-do 31116, Republic of Korea
J. C. Knowles
Division of Biomaterials and Tissue Engineering
UCL Eastman Dental Institute
Royal Free Hospital
Rowland Hill Street, London NW3 2PF, UK
M.-Y. Kim
Department of Oral and Maxillofacial Surgery
College of Dentistry
Dankook University
Cheonan 31116, Republic of Korea
D. Lee
Department of Oral Histology
Dankook University College of Dentistry
Cheonan 31116, Republic of Korea
H.-W. Kim, J.-H. Lee
Mechanobiology Dental Medicine Research Center
Dankook University
Cheonan 31116, Republic of Korea
H.-W. Kim, J.-H. Lee
Cell & Matter Institute
Dankook University
Cheonan 31116, Republic of Korea
H.-W. Kim
Department of Regenerative Dental Medicine
School of Dentistry
Dankook University
Cheonan 31116, Republic of Korea

FsL system (**Figure** 1A). The formation of FsL-induced periodic wave-form nanostructures emerges through ultrafast physical mechanisms initiated by ultrashort laser pulses[9] (Figure 1B and Note S2, Supporting Information). In detail, initial laser pulses generate sparsely distributed nanostructures that serve as scattering centers, enabling coupling of incident light with surface plasmon polaritons (SPPs) via diffraction. Continued irradiation enhances SPP excitation, creating interference between the linearly polarized laser field and excited SPPs that establishes periodic spatial modulation of energy deposition. This process initiates self-organization of transient, localized patterns that evolve into well-organized, extended periodic structures whose orientation is governed by laser polarization direction. Compared to long-pulse laser systems and other less-optimized FsL configurations, the optimized FsL parameters (230 fs per 10 µs) employed here enable the generation of significantly higher-density nanoscale wave-like features while suppressing undesired recast layer formation and debris deposition associated with thermal damage, thereby achieving superior spatial definition and enhanced morphological control for advanced biomedical applications.

Given that nanotopographical cues potently stimulate mechanotransduction, driving extensive transcriptional and phenotypic changes superior to well-defined microtopographies (Figure S1 and Table S3, Supporting Information),[5d,e,6c,10] we hypothesized the osteogenic potential of MSCs could be enhanced by modulating their nuclear architecture and chromatin reprogramming. To address this hypothesis, integrated nanoimaging and molecular biology techniques were applied to investigate the functional consequences of nanotexture-mediated nuclear deformation on MSC chromatin priming, transcription, and differentiation (Figure 1C). Results demonstrate nanotopography-microtubule-guided nuclear deformation as a promising chromatin priming strategy to control stem cell transcriptional identity and direct lineage commitment outcomes. This work elucidates nanotopography-induced nuclear remodeling as an approach to enhance regenerative capacity for next-generation titanium implant applications.

### 2.2. Comprehensive Characterization and Optimization of FsL-Induced Waveform Nanotextures on Titanium

Optimal FsL processing conditions were tailored to generate eco-friendly (strong acid-free) nanopatterning on Ti relevant for commercial manufacturing, considering processing efficiency, uniform nanotexture formation, mechanical stability, and safety requirements (Note S3, Supporting Information). FsL was exposed to the substrate surface in a 2D plane with a 30 µm gap and 500 mm $s^{-1}$ scan speed (15 $mm^2$ $s^{-1}$) to confer homogenous W-NT across the surface without cracks. The treatment process was demonstrated on both Ti grade 4 specimens and commercial dental implant fixtures, where the laser spot (yellow arrow) systematically traversed the surface to create uniform nanotextures (white arrow with blue line). The implant fixtures could be rotated 90° after processing to ensure comprehensive surface coverage, with treatment completion achieved within 3 s per quarter area (**Figure** 2A and Movies S1 and S2, Supporting Information). This treatment protocol generated distinctive periodic nanostructure peaks (peak height 211 ± 67 nm, pitch distance 0.89 ± 0.10 µm) with aligned rippling morphology compared to smooth control Ti surfaces with ≈181 nm etched depth per FsL treatment (Figure 2B,C; Figure S2, Supporting Information). Surface roughness analysis demonstrated four-fold higher average roughness (Ra 160 ± 7 nm) for W-NT versus control Ti (Ra: 46 ± 9 nm).

Systematic parameter optimization revealed critical processing windows for consistent nanotexturing on Ti (Figure 2D). Laser parameter optimization encompassed transverse overlap, vertical scanning speed, and power intensity (30 µm spacing, 500 mm $s^{-1}$, and 1W, respectively) to achieve uniform nanopatterning (Figures S3 and S4, Supporting Information), while insufficient or disrupted wave-form nanopatterning was observed under non-optimal conditions. Varying the FsL focal depth showed nanotexturing was achieved down to 4 mm below/up the basal focal plane, whereas more than 6 mm did not successfully pattern (Figure S5, Supporting Information). Since device surfaces can have curved anatomies, angle-dependent texture formation was examined, revealing decreasing roughness with angle shifts beyond 75° off-normal (Figure S6, Supporting Information). Applying multiple FsL scans, continuous unidirectional treatment heightened valley depths and roughness tenfold with disruption of the periodic waveform pattern. Additionally, bi-directional scanning introduced microscale tessellated grid patterns with turtle shell-like morphology (Figure S7, Supporting Information).

To demonstrate FsL versatility, we tested the technique across titanium substrates with varying surface roughness, as well as other metals, ceramics, and polymer biomaterials. Distinct nanowave-textures were also imposed on clinically-relevant computer numerical control machine-cut surfaces, distinct from commercially used surfaces (sandblasted, large grit, acid-etched implant surface (SLA)) with sporadic nano-holes and sharp micro-pits (Figure S8, Supporting Information). Nanowave-textures were conferred only onto metals (stainless steel, pure Gold (99.99%), Co-Cr alloy) – not ceramic (zirconia) or polymer (polytetrafluoroethylene), confirming the plasma-mediated mechanism specificity (Figure S9, Supporting Information). Together, this optimized FsL treatment can be used to homogenously generate W-NT nanotextures across Ti and other metal biomaterial surfaces.

Next, basic physicochemical characterization of FsL-treated Ti revealed slightly decreased hydrophilicity with reduced water contact angle and surface free energy, primarily attributed to polar component decreases from nanostructuring (Figure 2E; Figure S10, Supporting Information). Mechanical property assessment showed maintained structural integrity with adequate hardness and Young's modulus for biomechanical applications, outperforming commercially used SLA surfaces (Figures S11 and S12, Supporting Information). Crystallographic and chemical analysis confirmed preserved $\alpha$-Ti crystal phases with enhanced Ti-OH/C=O bonding (≈3% more) from controlled oxidation during non-thermal FsL processing (Figure 2F,G; Figure S13, Supporting Information). Minor variations in relative peak intensities near 40° between bare and FsL-treated samples likely result from preferred crystallographic orientation induced by the directional surface patterning.[11]

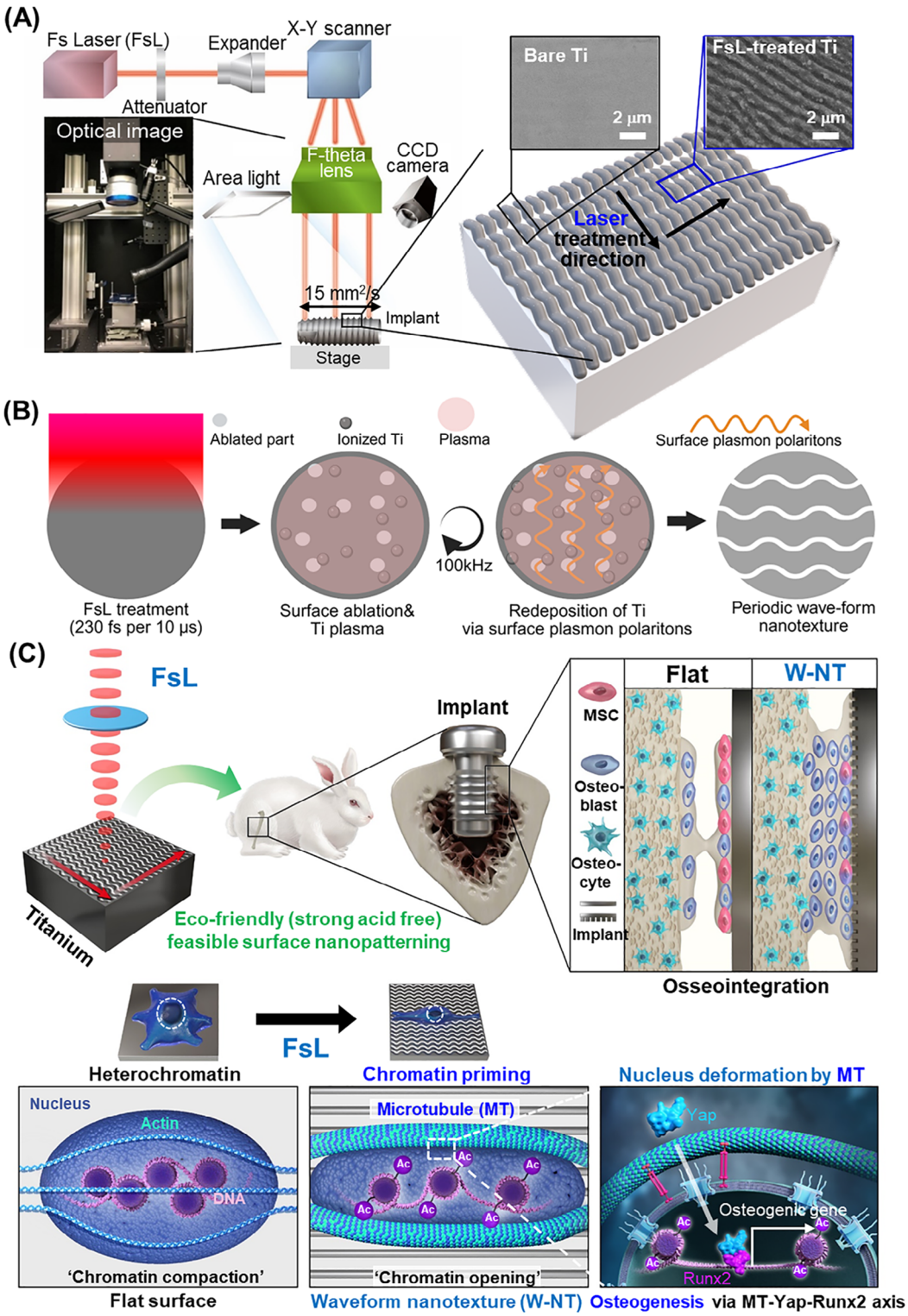


**Figure 1.** Eco-fabricated waveform nanotextures (W-NT) on titanium for driving nuclear deformation on bone regeneration. A) Schematic showing green-processed femtosecond laser (FsL) system (15 $mm^2$ $s^{-1}$) creating nanowave-textures (W-NT) on titanium (Ti) with potential for nuclear mechanotransduction and bone growth. B) Mechanism of FsL-mediated wave-form nanostructure fabrication. FsL treatment (1W, 230 fs, 100 kHz) ablates titanium surface, generating Ti plasma. Surface plasmon polaritons create periodic electromagnetic field patterns, leading to preferential material redeposition and formation of laser-induced periodic surface structures with characteristic wave-form nanotextures (W-NT). C) Proposed cascade initiated by nano-contact guidance deforming mesenchymal stem cells (MSCs) nuclei, altering chromatin programming toward euchromatin for sensitization to osteolineage commitment (called chromatin priming).

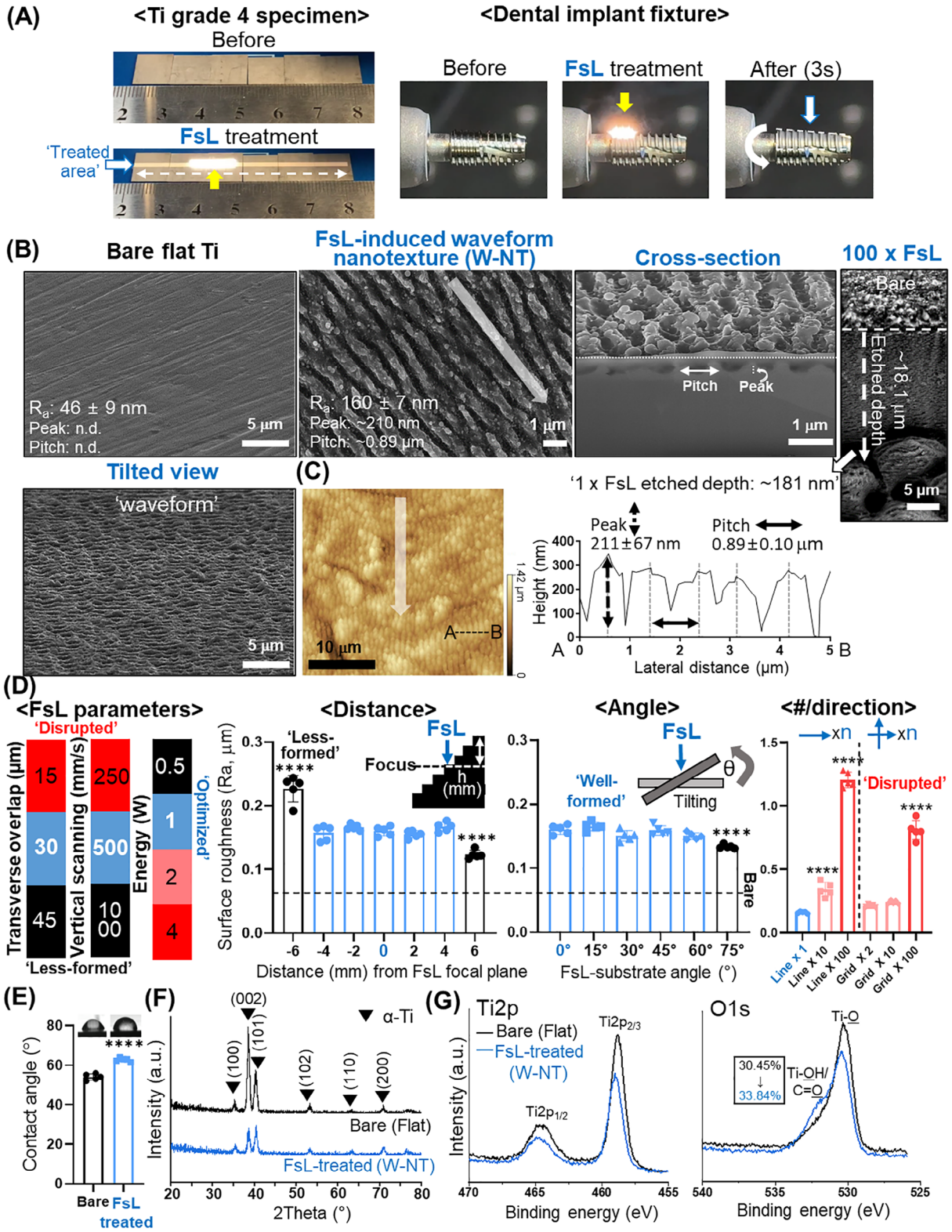


**Figure 2.** Characterization of FsL-induced waveform nanotexture on titanium surfaces. A) Visual documentation of femtosecond laser (FsL) treatment process. Left panels show Ti grade 4 specimens before and after FsL treatment with highlighted treated area (white arrow with blue line). Active laser spot indicated by yellow arrow. Right panels display titanium dental implant fixtures at various treatment stages (before, during FsL treatment with active laser spot indicated by yellow arrow, and after 3 s treatment). Treated area was marked by white dot line and pointed by the white arrow with the blue line. The implant fixture can be rotated 90 degrees for comprehensive surface treatment. B) Surface morphology comparison between bare flat Ti and FsL-induced

Collectively, these optimization studies with comprehensive characterization establish the refined FsL configuration as a robust, eco-friendly technique for precision nanotexture fabrication on metal biomaterials, with well-defined processing windows that enable scalable manufacturing for advanced medical device applications.

### 2.3. Nanowave Textures Confine Cell Morphologies with Enhanced Microtubules

MSCs respond to nanotopography by altering adhesion, morphology, and fate commitment.[12] To investigate these responses, rat bone marrow MSCs were evaluated over 24 h on W-NT versus flat Ti (machined-cut) controls. At initial attachment, smaller adherent areas with higher aspect ratios (length: width) emerged on W-NT (**Figure 3A**). By 24 h, W-NT further promoted aspect ratio elongation, with over 90% aligning to the nanogrooves (Figure 3B). A similar morphology was observed on W-NT-treated polished (ultra-smooth) Ti, distinguishing responses from conventional SLA topography (Figure S14, Supporting Information). Scanning electron micrographs verified alignment along nanotextures (white thin arrow), enabled by nanopodia (yellow arrow) into valleys (Figure 3C). Additional tests on FsL-treated nanotextures, varying the number of treatments (1–100 times) and direction (uni- or bi-directional), revealed an increased aspect ratio of cells corresponding to more pronounced peak-valley topologies (Figure S15, Supporting Information). For further analysis, single FsL treatment on 'machined-cut' Ti was selected as a clinically-relevant platform among various FsL treatment conditions, as it minimizes processing complexity while maintaining clinical applicability.

When adhesion-formable focal adhesion protein (Paxillin) was evaluated, W-NT exhibited higher overall paxillin expression, indicating strong cellular tension (Figure 3D). Detailed analysis of cell shape revealed reduced cytoplasmic widths at the nuclear center without prominent actin cables above nucleus, suggesting the involvement of other cytoskeletal components in regulating morphology (Figure 3E; Figure S16A, Supporting Information). Given their ability to sustain anisotropic strain, ascribed to unique stiffness and geometry, microtubules were examined.[13] Absolute tubulin expression was elevated in W-NT, without changes in post-translational acetylation or detyrosination marks (Figure 3F; Figures S16B and S17, Supporting Information), indicating that the key difference lies in the absolute amount and distribution of microtubules, rather than tubulin post-translational modifications on W-NT.[14] Together with enhanced focal adhesion, microtubule upregulation, and reorganization may contribute to higher force generation around nuclei on W-NT within 24 h, potentially influencing downstream differentiation trajectories over longer timescales.

### 2.4. Microtubules Activated by Nanowave-Textures Contribute to Nuclear Morphological Changes

Next, nuclear morphological responses on nanotopographical sensing were investigated. Within 6 h, MSCs on W-NT exhibited reduced 2D projected areas and nuclear shape index (NSI), alongside increased elongation, indicative of a shrunken ellipsoid morphology (**Figure 4A**). The coordinated cytoskeletal and nuclear alignment at 6 h hints at rapid nucleus-level perceptions of nanotextures. Strong correlations between nuclear area and NSI indicate distinct nuclear morphological changes on W-NT (Figure 4B). Further, 3D reconstructions verified reduced volumes yet increased z-axis heights, conferring less flattening (Figure 4C). Interestingly, The wavy nanopatterns of the W-NT surface were mirrored in the nuclear morphology, providing evidence for direct mechanosensing of nanotopographical features by the nucleus. Local force transmission from surface features to nuclei likely involves cytoskeletal linkages.[3c] Accordingly, F-actin, microtubule or intermediate filament disruption was individually tested using inhibitor treatments on W-NT (non-toxic 0.5 μM, latrunculin A, 10 μM nocodazole (Noco) or 2 μM withaferin A respectively). After 1 hr Noco exposure (microtubule inhibitor), nuclei reverted to round shape (higher NSI) with increased area and volumes, and disappearance of wavy nanopatterns on nuclei similar to those on a flat surface, implicating microtubules as key mediators for shaping nuclei (Figure 4D; Figure S18, Supporting Information).

waveform nanotexture (W-NT). SEM images reveal a smooth surface on bare Ti (Ra: 46 ± 9 nm with non-detectable peak and pitch parameters) versus distinctive aligned rippling patterns (white arrow) on W-NT surfaces (Ra: 180 ± 7 nm, Peak: ≈210 nm, Pitch: ≈0.89 μm). A Cross-sectional view shows characteristic peak-valley architecture with labeled pitch and peak features. An additional tilted view demonstrates the 3D "waveform" topography. 100× FsL treatment results in a deeper etched surface, revealing ≈181 nm etched depth per FsL treatment. C) Quantitative profile analysis of W-NT surface features. Atomic force microscope topographic mapping (left) and corresponding line profile measurement (right) reveal consistent periodic structures with peak heights of 211 ± 67 nm and pitch distances of 0.89 ± 0.10 μm. Aligned rippling patterns were highlighted by white arrow. D) Optimization parameters for FsL nanotexturing. Laser parameter optimization encompassed transverse overlap, vertical scanning speed, and power intensity (30 μm spacing, 500 mm $s^{-1}$, and 1W, respectively) to achieve uniform nanopatterning, while insufficient (black) or disrupted (red) wave-form nanopatterning was observed under non-optimal conditions. Surface roughness (Ra) analysis demonstrates: distance-dependent effects showing uniform texturing within ±4 mm from focal plane with significant degradation beyond 6 mm; angle-dependent effects maintaining consistent texturing up to 60° with significant decline at 75° substrate tilt angle; and treatment number and direction effects showing progressive Ra enhancement with increased treatment cycles (1× to 100× at same location) and further surface modification when combining perpendicular scanning directions (90° sample rotation followed by additional treatment cycles). The red color bar meaning overprocessed or disrupted group with non-uniform wave-nanopatterns. E) Contact angle measurements showing slightly decreased hydrophilicity of FsL-treated surfaces compared to bare Ti, resulting from the altered surface topography. F, G) Crystal structure assessment via XRD (F) and surface chemistry analysis via XPS (G). XRD analysis confirms preservation of the original titanium crystal phases after treatment, while XPS spectra reveal enhanced Ti-OH/C=O bonding (≈3%) on FsL-treated surfaces resulting from oxidation during non-thermal laser processing. Data are presented as mean ± SD ($n = 5$). Statistical significance was determined by t-test and one-way ANOVA with Tukey post hoc test (**$p < 0.01$, ***$p < 0.001$, ****$p < 0.0001$). In panel (D), statistical comparisons were made relative to the optimized FsL treatment condition (highlighted in blue at x-axis label).

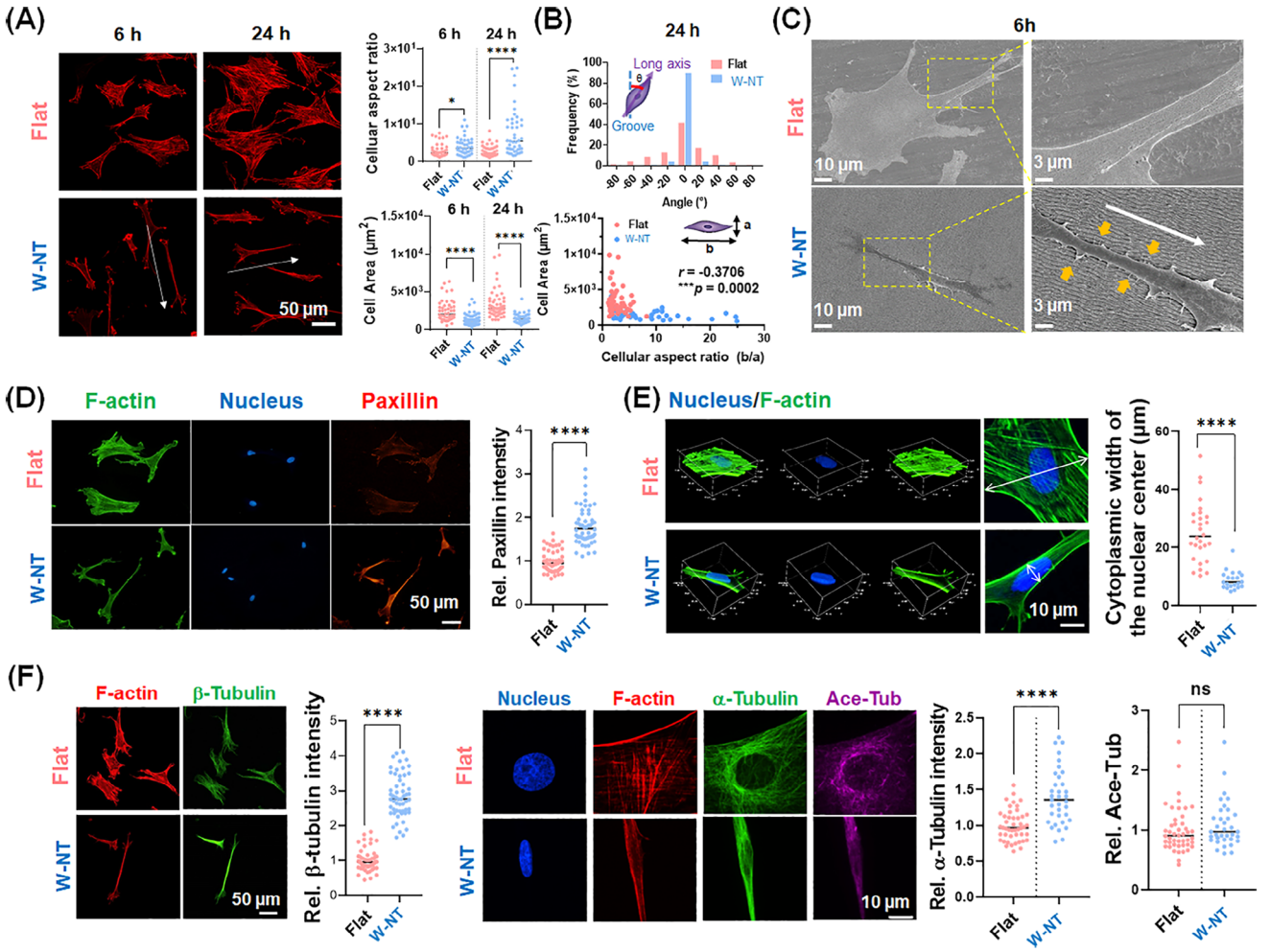


**Figure 3.** Nanowave-textures rapidly reorient MSC morphology with enhanced microtubules. A) Reduced cell areas with increased aspect ratios were observed on nanotextured titanium at 6 and 24 h. B) Over 90% alignment occurred along waveform direction by 24 h with sustained elongation. C) Scanning electron micrographs showed aligned adherens-type extensions into nanogroove valleys (white arrow) with nanopodia (yellow arrows) at 6 h. D) Enhanced overall paxillin expression indicated strengthened focal adhesions. Relative paxillin intensity normalized to average intensity from Flat. E) High-resolution 3D imaging revealed narrowed cytoplasmic widths (white arrow) at the nuclear center region with reduced actin cables over nuclei. F) Total microtubule levels selectively increased on nanotopographies without changes in acetylated tubulin. Together, these findings suggest that microenvironmental biophysical signals transmitted through focal adhesions, while microtubules may mediate the early nucleus-level detection of nano-cues. Statistical analysis was performed using Student's *t*-test (*$p < 0.05$, **$p < 0.01$, ***$p < 0.001$, ****$p < 0.0001$; ns, not significant). Unless otherwise mentioned, all experiments were conducted at 6 h post-seeding. The middle blank line represents the median value.

### 2.5. Nanowave Textures Induce Chromatin Opening, Mainly Increasing Histone Acetylation: Implication of Mechano-Priming MSCs for Osteogenesis

Related studies have connected surface-directed nuclear deformation to histone modifications that prime epigenetic programs.[15] Global chromatin patterns were thus probed here by immunolabeling acetylated histone H3 (AcH3), an open chromatin mark, using super-resolution imaging (N-SIM) under growth medium. W-NT enriched both AcH3 occupancy and nanodomain sizes, potentially enhancing lineage-specific responsiveness of MSCs under defined chemical cues by chromatin priming[16] (**Figure** 5A). Disconnecting surface cues from nuclei via Noco abolished the elevation of AcH3 level (Figure 5B). Furthermore, AcH3 expression showed a strong negative correlation with the nuclear shape descriptor ($r = -0.4311$), indicating that nanotopography-induced nuclear deformation significantly influences histone 3 acetylation (Figure 5B; Figure S19, Supporting Information). Taken together, a model emerges whereby nanotexture-directed cell orientation may transmit microtubule forces to reshape and prime nuclei, reprogramming closed chromatin into accessible landscapes (Figure 5C).

To validate nanotopography-induced chromatin priming, chromatin accessibility was mapped using assay for transposase-accessible chromatin sequencing (ATAC-seq) without osteogenic biochemical cues (Figure 5C; Figure S20, Supporting Information). MSCs cultured on W-NT exhibited selective promoter accessibility gains (60% increased vs 40% decreased) compared to other genomic regions (Figure 5D). Enhanced availability was observed in representative genes related to bone formation,

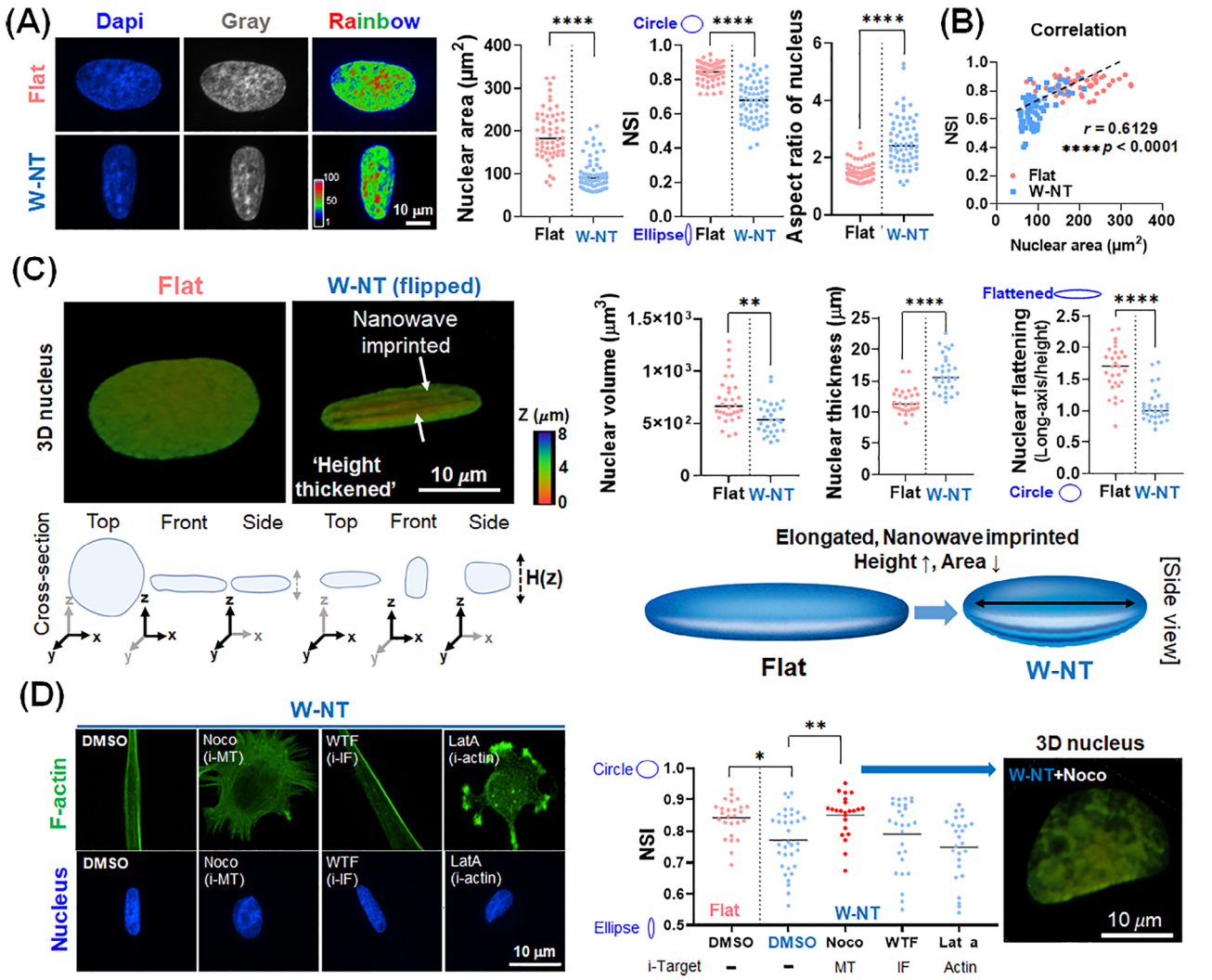


**Figure 4.** Microtubules activated by nanowave textures contribute to nuclear morphological changes. A) 2D analysis revealed reduced nuclear areas and shape indices (NSI) with heightened elongation (high aspect ratio) on nanostructured titanium. The inset shows the corresponding grey value scale for the rainbow-colored images. B) Nuclear area and NSI were tightly correlated in W-NT. C) 3D reconstructions showed reduced volume and flattening, with imprinting of wavy nanopatterns onto the nuclei. Schematic 3D nucleus image was shown. D) The microtubule inhibitor uniquely reversed nuclear geometry changes including wavy nanopatterns on the nucleus, induced by nanotopographies among cytoskeletal components. Statistics were performed using one-way ANOVA with Dunnett's post-hoc test or Student's *t*-test (*$p < 0.05$, **$p < 0.01$, ***$p < 0.001$, ****$p < 0.0001$). Middle blank line indicates the median value. withaferin (WTF) 2 μM, latrunculin A (Lat A) 0.5 μM, nocodazole (Noco) 10 μM were individually administered 1 h before fixation after 24 h of cell seeding onto W-NT for inhibiting intermediate filament (IF), F-actin (Actin), and microtubule (MT), respectively.

mechanosensing, and chromatin-remodeling genes (Figure S21A, Supporting Information). De novo motif analysis prioritized mechanotransduction and osteogenic transcription factors (POL003.1, *RUNX2, TEAD2*) from differentially accessible sequences (Figure 5E; Figure S22B, Supporting Information). Gene ontology (GO) enrichment analysis revealed W-NT-upregulated promoters associated with osteogenesis (e.g., cellular response to dexamethasone stimulus, Wnt signaling pathway, post-embryonic development, hard plate development, positive regulation of osteoblast differentiation), microtubule-related mechanotransduction (e.g., neuron projection extension, cytoskeleton organization, nucleus organization, axon guidance), and chromatin-opening (e.g., positive regulation of transcription, RNA polymerase II promoter, histone H3-K14 acetylation)[17] (Figure 5F). Over half (57–70%) of tested promoters associated with these pathways exhibited selective chromatin opening on W-NT (Figure 5G). Collectively, integrative ATAC-seq analysis suggests that nanotopography-mediated nuclear deformation primes chromatin accessibility, favoring osteogenesis through mechanotransduction.

### 2.6. Mechano-Primed MSCs Exhibit Enhanced Osteogenic Transcriptional Responsiveness Upon Biochemical Inputs

To assess whether nanotopography-mediated chromatin modifications enhance osteogenic transcriptional responsiveness under defined biochemical cues, transcriptional profiling (RNA-seq)

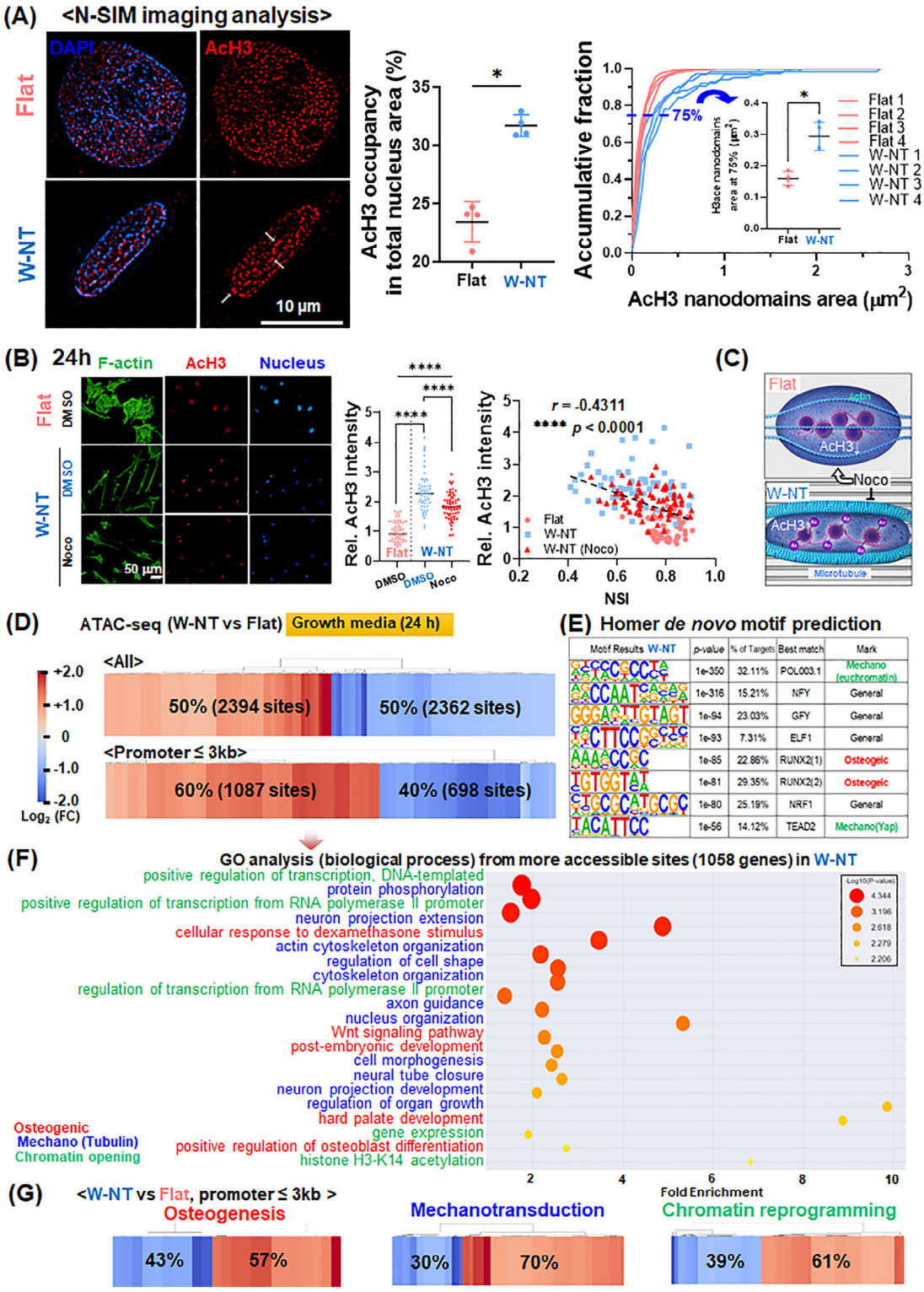


**Figure 5.** MSCs primed on nanowave-textures undergo chromatin remodeling to support osteogenic fate without biochemical cue. A) Super-resolution imaging (N-SIM) revealed increased acetylation of histone H3 (AcH3, a euchromatin mark) occupancy and domain sizes on nanotextured (W-NT) surfaces compared to flat Ti surfaces. Middle blank line in graphs represent mean values. Large AcH3 domains were indicated by arrow in W-NT. B) Microtubule disruption using nocodazole (Noco) attenuated nanotopography-induced AcH3 levels and nuclear shape changes. The middle blank line on AcH3 intensity graph represents the median value, and the dashed black line indicates the trend line. Signal intensities were normalized to the average values obtained from Flat (DMOS). C) Proposed mechanism where aligned cell elongation transmits microtubule forces to deform nuclei, en-

was conducted in the presence of osteogenic differentiation media up to 3 days (**Figure 6A**). Heatmap and distance-based clustering of differentially expressed genes (DEGs) displayed maturation stage-dependent patterns, with nanotextures substantially reshaping the transcriptome at days 1 and 3 probably due to chromatin priming effects (Figure 6B,C). GO analysis connected upregulated day 1 DEGs to osteogenesis, mechanotransduction, and chromatin reprogramming in nanotexture[18] (Figure 6D). Co-upregulated genes between days 1 and 3 maintained similar associations (Figure S22, Supporting Information). Downregulated pathways linked to lipid or fatty acid formation, reinforcing osteolineage redirection (Figure S23, Supporting Information). Further, transcriptome clustering for nanopatterning, osteogenic biochemical cues, and their synergistic effects argued synergism between physical and biochemical cues (Figure S24, Supporting Information). Indeed, ossification, microtubule, mechanotransduction-related, chromatin remodeling gene subsets showed enrichment on nanotopographies, increasing over time (Figure 6E). Transcription factor motif analysis implicated CTGF as a candidate mechano-regulator based on altered chromatin accessibility and transcripts, which is a well-known mechanotransducer: YAP-TEAD[19] (Figure S25, Supporting Information; Figure 6E). RUNX2 and downstream osteogenic markers such as ALP, BSP, and OCN were upregulated over 10–150 fold on W-NT, validated by enhanced biomineralization (Figure 6F,G). Disrupting mechanotransduction via microtubule inhibitor blunted RUNX2, OCN, and biomineralization (Figure 6H). Taken together, results demonstrate nanotexture-mediated nuclear priming into euchromatic status elevate osteogenic transcriptional activity in a microtubule-dependent manner under defined biochemical cues.

### 2.7. Nanowave-Textures Orchestrates Osteogenesis Through Microtubule-Mediated Nuclear Mechanotransduction and Chromatin Modification

Given implicated roles for the mechanotransducer YAP and osteogenic driver RUNX2 under osteogenic biochemical cues,[20] subcellular localization was examined on nanostructured surfaces with inhibitors to unveil the biochemical cascades along with mechanotransduction. Both (co)transcription factors displayed greater nuclear enrichment on W-NT, accompanied by heightened H3 acetylation (**Figure 7A–C**). The YAP inhibitor verteporfin (VP) attenuated YAP nuclear localization and AcH3 levels without affecting RUNX2 (Figure 7A–C). Similarly, the AcH3 inhibitor (C646) reduces YAP nuclear ratios but not RUNX2 (Figure 7D–F). Furthermore, a significant correlation ($r = 0.5780$) occurred between YAP nucleus localization and its AcH3 levels (Figure S26, Supporting Information). Combined, YAP and AcH3 bidirectionally regulate each other's nuclear activity on nanotopographies independently of RUNX2.

To investigate the mechanotransduction axis involving three mechano-reactive components including RUNX2, we disrupted microtubules, the most upstream component of mechanotransduction, using Noco treatment on nanowave-textured surfaces. Microtubule disruption compromised all revealed downstream mechanotransduction signaling, including nuclear enrichment of both YAP and RUNX2 (Figure 7G,H) and AcH3 expression previously observed in Figure 5B. The nuclear/cytoplasmic ratio of YAP and RUNX2 showed significant correlation with microtubule organization and nuclear shape index (Figure 7I), demonstrating that microtubule-mediated nuclear deformation functions upstream to regulate both nuclear import of (co)transcription factors and chromatin remodeling on W-NT.

Together with the attenuation of enhanced osteogenic effects using YAP or AcH3 inhibitors (Figure 7J–L; Figure S27, Supporting Information), results argue a multi-tiered cascade initiated by nanotopographies (W-NT). This cascade proceeds through microtubule reorganization, which triggers nuclear deformation, leading to coordinated YAP activation, chromatin remodeling (AcH3), and RUNX2-mediated osteogenic regulation ('Nanotexture (W-NT)' - 'Microtubules' - 'Nucleus deformation' – 'Yap, AcH3 and RUNX2 activity'), with YAP and histone acetylation exhibiting bidirectional interaction. While actomyosin tension played only subordinate roles (Figure S28, Supporting Information),[21] the microtubule-nucleus-'YAP-chromatin-RUNX2' axis emerges as a critical mediator translating biophysical cues (W-NT) into chromatin spatiotemporal dynamics that direct cell function.

### 2.8. Nanowave-Textured Implants Stimulate In Vivo Osteogenesis and Bone Formation

To investigate early cell-implant interactions in vivo, we first examined peri-implant tissue responses in a mouse tooth model (**Figure 8A**). Titanium miniscrews (Ø 1 mm, height 1.42 mm, grade 4 titanium) with either untreated (Flat) or femtosecond laser-textured (W-NT) surfaces were implanted into tooth defects ($n = 3$ per group, Figure S29 and Movie S2, Supporting Information) following bone healing, 4 weeks after tooth extraction. Two weeks post implantation, analysis of the outermost peri-implant cells demonstrated that W-NT surfaces induced significant mechanotransduction responses, characterized by elevated $\alpha$-tubulin expression, reduced Nuclear Shape Index (NSI), increased nuclear YAP localization, and enhanced histone H3 acetylation compared to Flat controls (Figure 8A; Figure S30, Supporting Information). These in vivo results corroborate our in vitro findings on mechanotransduction activation.

hancing chromatin accessibility. D) ATAC-sequencing under growth media (24 h, without osteogenic biochemical cues) demonstrated selective opening of promoters on W-NT compared to flat surfaces. Heatmaps show differential chromatin accessibility across all genomic regions and promoter-specific regions (<3 kb). E) De novo discovered motifs (POL003.1, *RUNX2, TEAD2*) were linked to mechanically activated and osteogenic transcription factors. F) Gene ontology (GO) analysis connected differentially accessible genes to osteogenesis, microtubule-related mechanotransduction, and chromatin opening. G) Over 50% (57–70%) increased accessibility occurred at tested promoter (≤3kb) subsets related to these pathways. Ossification (GO0001503), mechanotransduction (GO0003924, GO0007266, GO0005874), and chromatin remodeling (GO0006338)-related genes differentially accessible by nanotexture. Fold change>1.5. Statistics analysis were performed using one-way ANOVA followed by Tukey's multiple comparison test, or non-parametric Mann–Whitney test for pairwise comparisons (*$p < 0.05$, ****$p < 0.0001$).

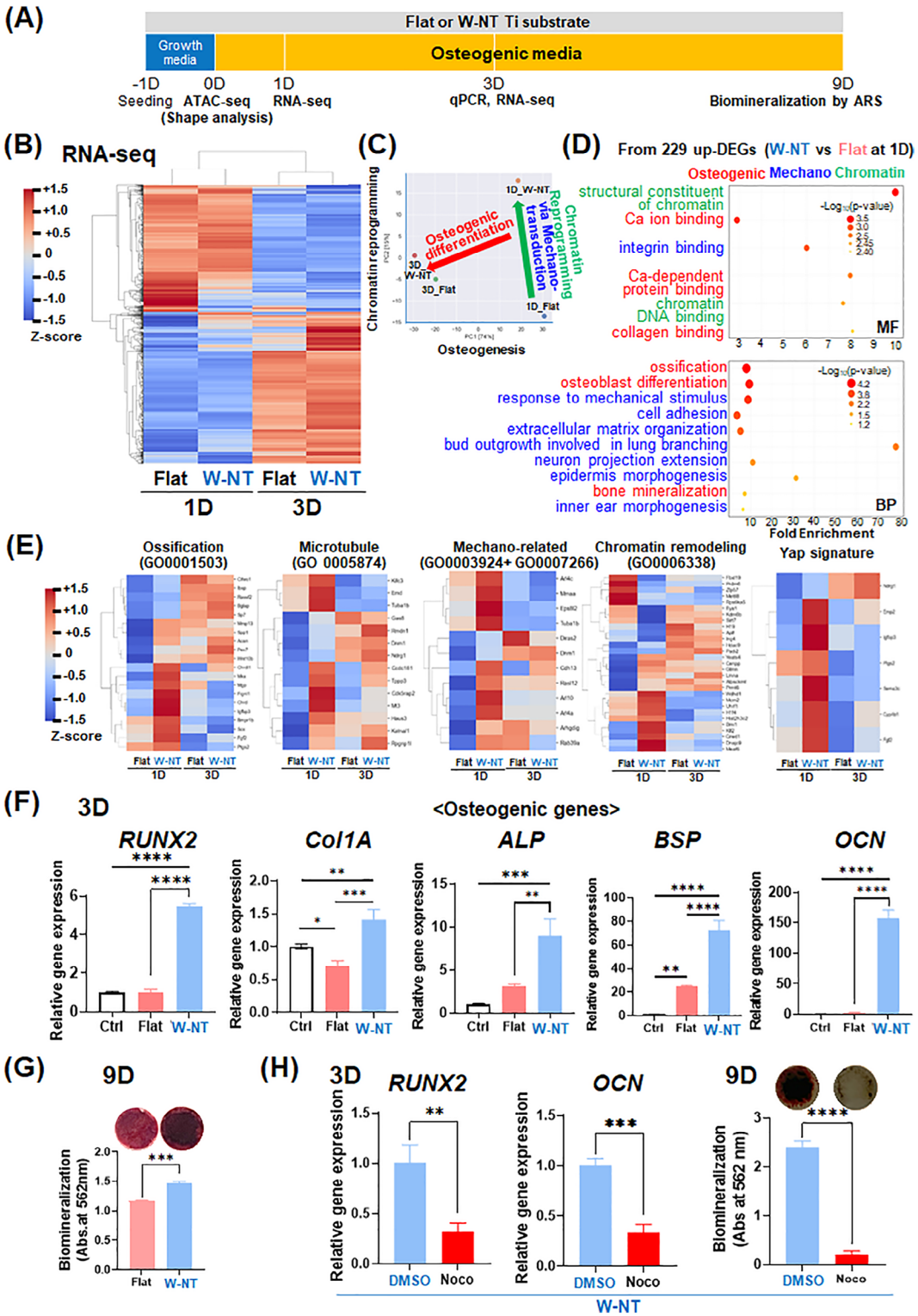


**Figure 6.** Osteogenic transcriptional responsiveness of MSCs was enhanced under biochemical cues on nanowave-textures. (A) Experimental timeline. Molecular analyses were performed at day 1 (D1) and day 3 (D3) of osteogenic induction. Biomineralization was examined after 9 days (D9). The bracket below D0 indicates time point of key studies presented in previous figures. (B) Distance-based clustering of differentially expressed genes (DEGs) (fold change > 1.5) from RNA sequencing of MSC cultured on D3 nanotextured (W-NT) and D1 flat titanium substrates. (C) Principal component analysis (PCA) confirmed transcriptomic divergence across biochemical induction timepoints and surface topologies. (D) Gene ontology enrichment linked D1 W-NT upregulated genes to osteogenesis (red), mechanotransduction (blue), and chromatin reprogramming (green). BP (biological process),

The osteoinductive capacity of wavy nanotextures was evaluated in a rabbit tibia model. W-NT implants were fabricated with grade 4 titanium 'machined cut' screws and benchmarked against bare 'machined cut' and commercially available golden standard "SLA" controls (Figure 8B). First, we conducted mechanical anchorage analysis in artificial bone blocks mimicking alveolar bone density (Figure S31A, Supporting Information). The W-NT implants required significantly higher insertion torque to reach standardized depth due to their enhanced surface roughness (Figure S31B, Supporting Information). However, it demonstrated comparable initial stability metrics to Flat surfaces (Figure S31C,D, Supporting Information), likely due to their identical macroscale thread geometry, with both outperforming SLA implants due to the slightly reduced effective thread diameter of SLA.[22]

Despite their significantly different surface roughness and morphology (Ra of ≈0.16 µm for W-NT vs ≈1.4 µm for SLA, Figure S8, Supporting Information) with different cell adhesion behaviors (Figure S14, Supporting Information), comparable in vitro biomineralization was observed between W-NT and SLA groups, with both outperforming the bare Ti control (Figure S32, Supporting Information). Cortical defects were generated in bilateral tibias, receiving one screw type each (Ø 3.4 mm, $h = 6$ mm) by round-robin assignment for randomization ($n = 7$). After 4 weeks implantation, histology displayed direct bone-implant contact without inflammation (score 0) across all groups, validating surgery success. In line with this, hemolysis testing with rat red blood cells and alveolar tissue biocompatibility evaluation under oral-bacteria-exposed conditions confirmed excellent biocompatibility of the nanotopography similar to non-treated control (Figure S33, Supporting Information).

Meanwhile, ≈20% more bone-implant contact and area, which are vital quantitative metrics clinically used to assess implant osseointegration and efficacy, were discerned over the initial two screw threads for W-NT and SLA versus machined Ti controls (≈66% screw length analyzed, $n = 14$) (Figure 8C; Figure S34, Supporting Information). µCT 3D reconstructions further visualized peri-implant 3D bone formation surrounding W-NT and SLA screws in cortical and marrow regions (Figure 8D).

In total, in vivo data corroborate in vitro osteogenic priming by nanoscale waveform cues via replicated bone growth, achieving parity with high-performing SLA. To our knowledge, this represents the first investigation of surface nanotexture-driven osseointegration using facile, upscalable femtosecond laser nanotexturing. Beyond providing a platform for bone regenerative applications, results more broadly demonstrate the potency of biophysical engineering to directly instruct cell function.

## 3. Discussion

In summary, we present a robust, scalable, green-processed femtosecond laser approach for generating homogeneous nanowave textures on diverse metal biomaterials with an industrial throughput of 15 $mm^2\ s^{-1}$. Key findings include: i) Optimized FsL processing at 15 $mm^2\ s^{-1}$ with 1W (10 µJ with 100 kHz) enables reliable large-area nanostructuring while characterization of focal angle and height dependencies provides guidelines for quality control. Importantly, the textures confer biofunctional cues without compromising bulk mechanical integrity. ii) Rapid morphology and nuclear adaptations of mesenchymal stem cells on wave patterns, including alignment, elongation, and microtubule accrual, implying early topology-mediated chromatin priming within 24 h in the absence of biochemical cues. iii) At molecular and functional levels under osteogenic biochemical cues, nanowave cues drive osteogenesis through a microtubule-YAP-chromatin axis that connects biophysics to epigenetics. iv) In vivo osteogenic capacity confirmed through a step-wise animal model approach: early mechanotransduction (enhanced H3ac, α-tubulin, nuclear YAP) demonstrated in mouse tooth implants at 2 weeks, followed by robust bone formation in rabbit tibial defects at 4 weeks, where nanowave-textured implants achieved comparable bone-implant contact (≈20% increase) to clinical SLA controls over machined surfaces. To our knowledge, this provides first evidence that green-processed femtosecond laser nanopatterning on metal can induce bone regeneration while exemplifying chromatin engineering via biophysical tools. Importantly, the scalable nanofabrication and mechanistic insights pave the way for translating nanotopography technologies to enhance osseointegration. More broadly, findings reveal potent intersections between materials science and mechanobiology that can be harnessed for regenerative medicine by instructing stem cell fate.

While our FsL processing approach demonstrates robust biological efficacy, it is important to acknowledge the technical constraints of this nanofabrication method. Our systematic investigation of scanning parameters revealed that the uniform periodic waveform pattern with 0.89 µm pitch and 210 nm peak represents a unique morphology achievable under our optimized processing conditions (1W, transverse overlap 30 µm, vertical scanning 500 mm $s^{-1}$) from 1030 nm wavelength with 230 fs pulse duration. Alternative scanning strategies either compromise the uniformity of the periodic waveform or introduce unwanted microscale features that deviate from the optimized submicron regime. The consistent 0.89 µm pitch appears intrinsically linked to the laser-material interaction at our specific parameters, which were constrained by commercial femtosecond laser system specifications and industrial requirements. Achieving fundamentally different pattern profiles at equivalent length

MF (molecular function). (E) Specific functional gene sets (osteogenic, microtubule-mediated mechanotransduction, chromatin remodeling, and Yap signature) exhibited greater enrichment on nanotextured surfaces compared to flat surfaces, with further increases observed over time. (F) qPCR analysis validated significantly elevated expression of osteogenic lineage markers (osteogenic transcription factor (RUNX2), Early (Col1, ALP, BSP), and late (OCN) osteogenesis) on W-NT. The control group is 1 day culture on the flat substrate under growth media, and all data were compared to control (1) after GAPDH normalization. Statistics without indicators are compared to control. (G) Enhanced biomineralization at D9 on W-NT was visualized using Alizarin Red S staining. (H) Microtubule inhibitor (nocodazole (Noco)) attenuated the expression of osteogenic genes and reduced biomineralization even in the persistent nanotopography. Statistics were performed Student's *t*-test (two-sided, two groups) or one-way ANOVA followed by Tukey's multiple comparison test ($*p < 0.05$, $**p < 0.01$, $***p < 0.001$, $****p < 0.0001$). Data are presented as mean ± standard deviation (SD) for (F–H) ($n = 3$).

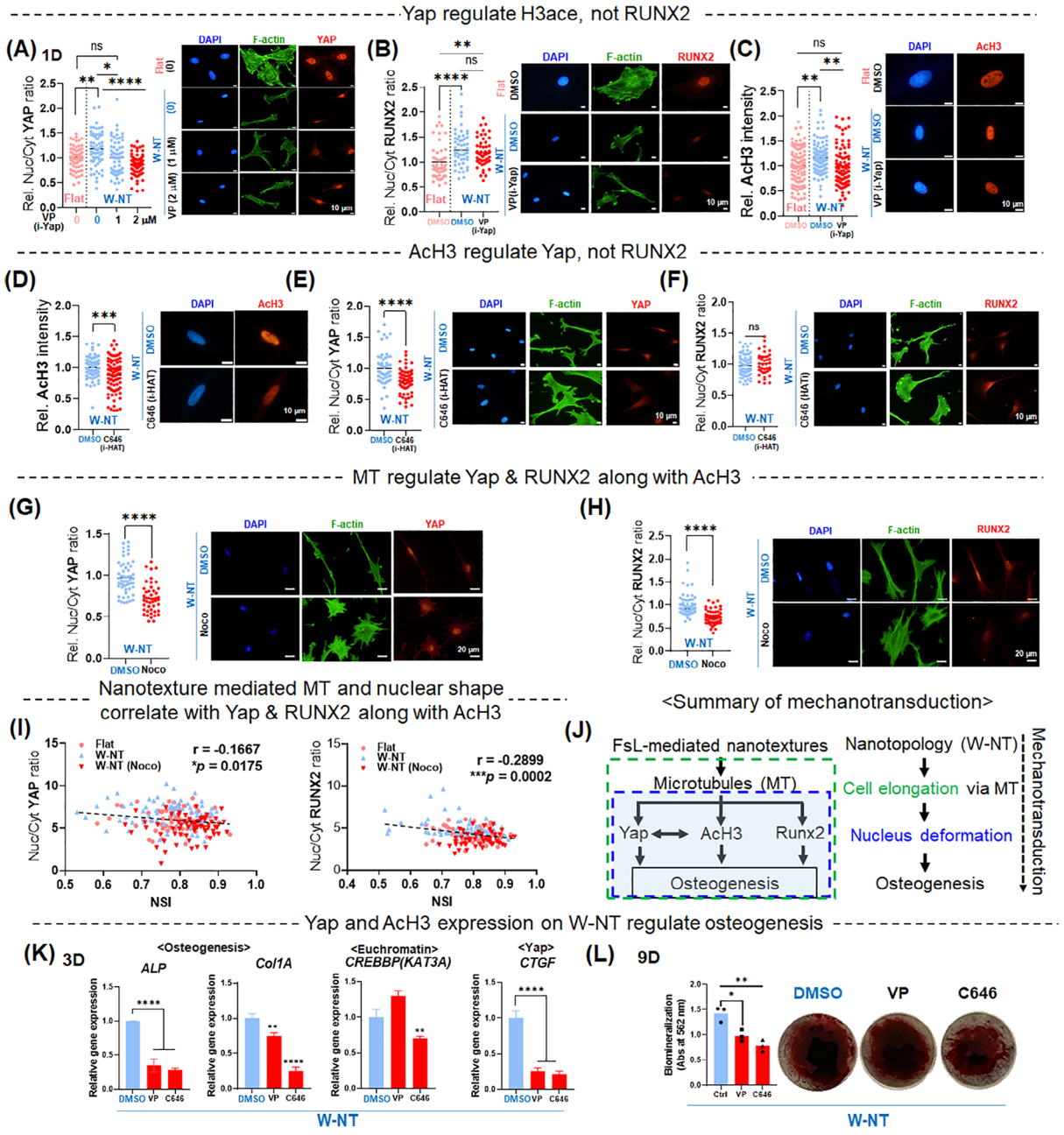


**Figure 7.** Nanowave-textures directs osteogenesis through microtubule-mediated nuclear mechanotransduction and chromatin modification. (A–C) Relative nuclear/cytoplasmic (Nuc/Cyt) ratios of YAP and RUNX2, and histone 3 acetylation (AcH3) in MSCs cultured on nanotextured titanium for 24 h under osteogenic biochemical cues, with/without the YAP inhibitor verteporfin (VP). VP attenuated YAP activity and AcH3 levels without affecting RUNX2. (D-F) AcH3 inhibitor (C646) reduced YAP but not RUNX2 nuclear accumulation on nanotopographies. (G&H) The microtubule inhibitor nocodazole (Noco) abolished nanotopography-induced nuclear enrichment of YAP and RUNX2, despite persistent nano-cues. (I) Significant relationships were identified between Nuc/Cyt ratios of YAP or RUNX2 and nuclear shape index, linking deformation of nucleus to YAP and RUNX2 activity on W-NT. Microtubule disruption by Noco attenuated these W-NT-mediated effects. (J) Proposed cascade initiated by nanotopographical sensing where microtubules remodel nuclei to activate the YAP-chromatin signaling axis directing RUNX2 nuclear import and osteogenesis ('Nanotexture (W-NT)' - 'Microtubule' - 'Nucleus deformation' - 'Yap, histone acetylation and RUNX2 activity'). (K,L) Molecular inhibition of cascade components profoundly reduced osteogenic gene expression (K, day 3) and biomineralization (L, day 9). Genes investigated include osteogenic markers (*COL1* and *ALP*), a histone acetyltransferase (*KAT3A*), and a Yap target gene (CTGF) under each inhibitor. All experiments were performed after 1 day of osteogenic differentiation unless otherwise specified. Inhibitors (C646, 10 μM; VP, 2 μM; or Noco, 10 μM) were added 1 h before fixation for (A-K). For 3-day (D3) and 9-day (D9) differentiation experiments (K&L), C646 and VP were included in the differentiation media, while Noco was added 1 h before each media change. Data are presented as mean ± standard deviation (SD) for biological triplicate experiments. The middle blank line on bar graphs indicates the median value. Student's *t*-test (two-sided, two groups) or one-way ANOVA with Tukey's multiple comparisons test was used (*$p < 0.05$, **$p < 0.01$, ***$p < 0.001$, ****$p < 0.0001$; ns, not significant). Pearson correlation was performed for (I).

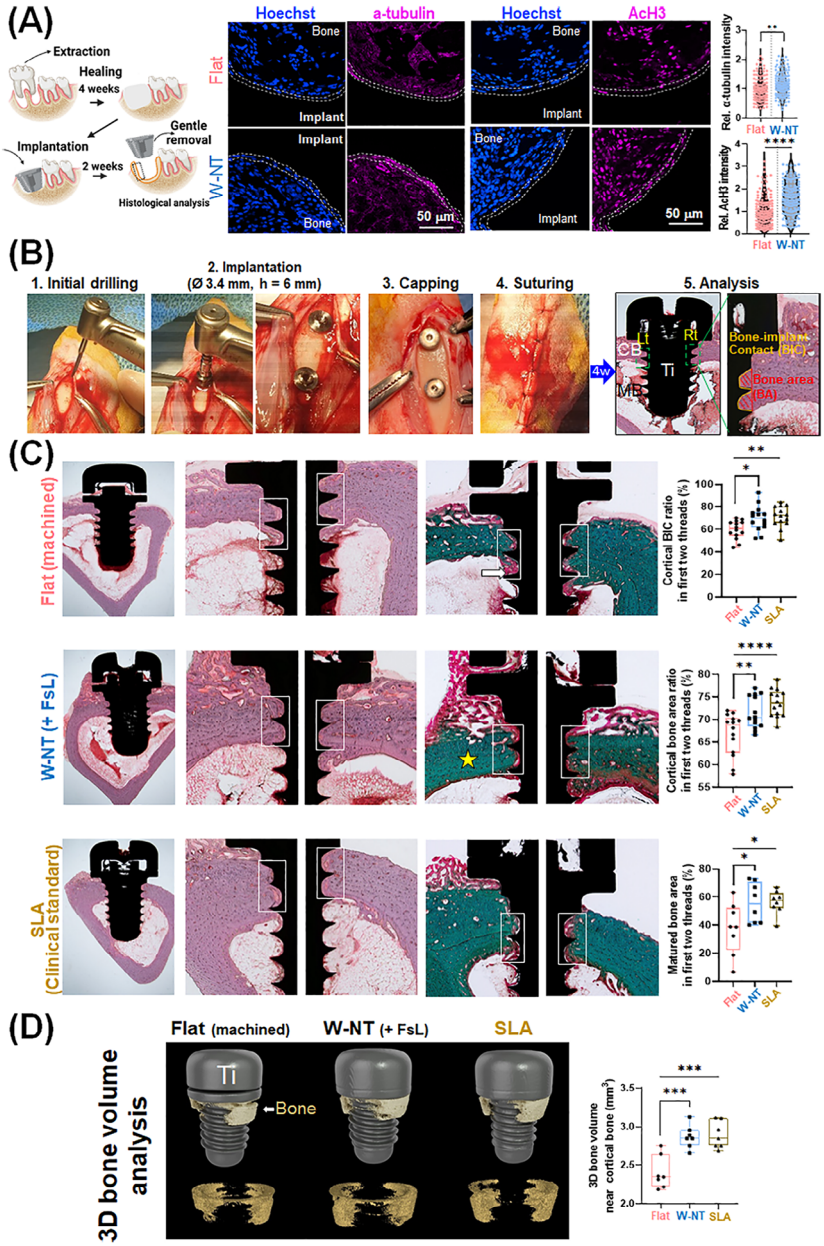


**Figure 8.** Nanowave-textured titanium implants promote bone regeneration comparable to clinical standard surfaces. (A) Mouse tooth defect model ($n = 3$) with titanium miniscrew implants (Ø 1 mm, height 1.42 mm) comparing untreated (Flat) and green-processed femtosecond laser-textured (W-NT) surfaces. Immunofluorescence analysis at 2 weeks post-implantation shows enhanced histone H3 acetylation and $\alpha$-tubulin expression in cells adjacent to W-NT surfaces. Quantification was performed using two randomly selected images per implant, excluding the bottom of the screw. Each data point represents an individual cell, with white dots indicating the outermost cells in direct contact with the implant surface. Signal intensities were normalized to the average values obtained from Flat. (B) To evaluate bone regeneration efficacy, bilateral tibia round defects were generated in rabbits ($n = 7$), with one of three titanium implant screws (Ø 3.4 mm, $h = 6$ mm) randomly assigned to each defect: femtosecond laser (FsL)-textured, standard "machined" or "sandblasted/acid-etched (SLA)." (C) Percent bone-implant contact (BIC) and bone area (BA) were quantified from H&E-stained histology over the first two screw threads within cortical bone ($n = 14$ implants). FsL and SLA groups showed ≈20% greater BIC and BA compared to untreated machined surfaces. Masson's trichrome staining further confirmed greater mature bone formation (green/yellow) around FsL and SLA screws ($n = 7$). (D) 3D reconstructions of peri-implant regions from µCT data corroborated enhanced cortical and trabecular bone ingrowth around FsL and SLA screws. Statistics were performed using Student's $t$-test (two-sided, two groups) or one-way ANOVA with Tukey's multiple comparison test (*$p < 0.05$, **$p < 0.01$, ***$p < 0.001$, ****$p < 0.0001$). Box plots depict data distribution through quartiles (Q1, median, Q3) in the box, with whiskers representing minimum and maximum values, and individual dots showing all data points.

scales would necessitate modification of core laser parameters, representing a limitation of the current approach. However, this constraint does not diminish the biological significance of our findings, as the single optimized nanowave pattern consistently demonstrates potent osteogenic capacity across multiple experimental models, suggesting that the observed biological effects are tied to precise geometric parameters achievable through this particular laser processing regime.

## 4. Experimental Section

*Green-Processed Femtosecond Laser System and Treatment*: Laser-induced periodic surface structures were fabricated on the surface of the specimen using a homemade femtosecond YB:KGW chirped pulse amplification laser. The Gaussian laser pulses with center wavelength of 1030 nm, pulse repetition rate of 100 kHz, pulse duration of 230 fs (per 10 µs) and maximum output power of 1 W (10 µJ) were optimally set. The pulse energy was controlled by the combination of a thin-film polarizer and a half-wave plate mounted on a motorized rotation stage. The laser beam was magnified as twice and then it was focused at the sample by XY galvano scanner and an F-theta lens (IntelliSCAN III 14, Scanlab, Germany). The focused beam spot size was 30 µm. An electro-optic modulator in the chirped pulse amplification laser was used as a laser pulse shutter and synchronized to the machining system. The sample was mounted on a computer-controlled Z-axis stage and illuminated with area lights to enable monitoring the machining process with a camera. Figure 1a shows the schematic illustration of FsL systems. All surfaces were treated with a laser scanning speed of 500 mm $s^{-1}$. The processing system was set so that the length of Rayleigh was at least 10 mm after consideration of the height difference between peak and valley of the screw specimen for in vivo. The medical grade, grade 4 Ti disk specimen (Ø = 10 mm, $h$ = 2 mm, TITANIUM TTi, Hwaseong, Korea) was selected for FsL treatment. They were polished using a polisher (LaboPol-5, Strouers, Ballerup, Denmark) with 220 grit SiC papers or serially polished from 220 to 4000-grit SiC papers to have high-polishing surface. After polishing, specimen were ultrasonically cleaned with acetone, ethlene alchol, and deionized water for 10 min sequentially. FsL treatment was also performed on grade 5 Ti (TITANIUM TTi, Hwaseong, Korea), gold (Woori Dongmyung, Seoul, Korea) and zirconia (Genoss, Suwon, Korea) disk specimens (Ø = 10 mm, $h$ = 2 mm). The FsL laser intensity (0.5–4 W), transverse scanning overlap (15–45 µm), vertical scanning speed (250–1000 mm $s^{-1}$), type (line or grid), and the number of treatments (1, 50, or 100) were adjusted to vary the topology. Depending on the surface position (from –6 to +6 mm) from the FsL focusing basal level (0 mm) and angle from the FsL focusing basal plane from 0 to 75°, nanotexture was investigated.

*Surface Analysis*: The specimens were coated with Au, and scanning electron microscopy (SEM, Sigma 300, Carl Zeiss, Germany) images were captured.[13b] For cross-sectioned images, a focused ion beam 2 (JEOL. LTD., JIB-4601F, Akishima, Tokyo, Japan) was utilized with SEM. The hydrophilicity of the specimen surfaces was measured by contact angle analysis using a Surface Electro Optics instrument (PHX300, SEO, Suwon, Korea) and distilled water (10 µL and $n$ = 5). Surface energy was calculated by Owens–Wendt methods based on contact angle results from distilled water and ethylene glycol (10 µL and $n$ = 5), which use non-polar (dispersive) and polar components of each solution for analysis.[23] For hardness, surface local stiffness, and roughness (Ra, arithmetical mean) analysis, nanoindenter (TI 750 Ubi, Hysitron, Minneapolis, MN, USA) and 3D surface confocal laser scanning microscope (Carl Zeiss, LSM 800, Germany) were utilized. Nanoindentor using Berkovich tip was loaded to the surface for 5 s up to 2000 µN, held for 2 s, and unloaded for 5 s. For evaluating topology in detail, atomic force microscope (SPM-9700, Shimadzu Corporation, Japan) with XY/Z resolutions of 0.2 and 0.01 nm were adpated. FsL-treated titanium samples were analyzed under ambient conditions using contact mode with silicon nitride cantilevers. Line profile measurements were extracted from 10 µm × 10 µm scan areas to quantify peak heights and pitch distances. Peak heights were measured as the vertical distance from valley to summit, while pitch distances were defined as center-to-center spacing between consecutive peaks. XRD (Rigaku, Tokyo, Japan, Cu K$\alpha$, 40 mA, 45 kV, from 20° to 80° of 2$\theta$ with a sampling width (0.02°) and scan speed (0.5°/min)) and XPS (K-alpha, Thermo Scientific, Waltham, MA, USA, Al K$\alpha$ source (1486.6 eV), voltage (12 kV), emission current (3mA)) were performed to analyze phase and chemical bonding of surface. The peak of C 1s at 284.8 eV was used as a reference.

*Cell Adhesion, Morphology, and Protein Expression Analysis*: Bone marrow-derived MSCs were isolated from 5-week-old male Sprague–Dawley rats as described previously.[24] All protocols involving animals were approved by the Animal Care and Use Committee of Dankook University (Approval no: DKU-18-032). The rat femora and tibiae were cut at the proximal and distal epiphyses, placed vertically in a 1.5 mL microtube, and centrifuged at 2000 rpm for 3 min to collect the bone marrow. The bone marrow was suspended with pipetting in growth medium (GM, $\alpha$-MEM supplemented with 10% fetal bovine serum containing 1% penicillin/streptomycin (P/S)), filtered by cell strainer, and then centrifuged at 200 g for 5 min. The resulting cell pellet was resuspended and plated in a culture dish, incubated under a humidified atmosphere of 5% $CO_2$ in air at 37 °C. Nonadherent hematopoietic cells were removed from the medium during medium changes, and the cells that had undergone three passages were used for further experiments. The cells were screened for mycoplasma contamination, and no mycoplasma was detected.

To observe cellular and nuclear differences among materials, 1000 rMSCs (passages 3–6) were seeded onto Ø10 mm disk specimens and cultured for 6 or 24 h. After fixation with 4% paraformaldehyde (PFA), permeabilization with 0.3% Triton X-100, and blocking with 5% bovine serum albumin (BSA), the cells were incubated overnight at 4 °C with primary antibodies diluted in 0.3% Triton X-100 containing 1% BSA, as detailed in Table S4 (Supporting Information). The following day, after washing with PBS, secondary antibodies were applied for 1 h, as described in the same table. Subsequently, the cells were stained for F-actin and the nucleus using phalloidin (A12379/A22283, Alexa Fluor™ 488/546, Thermo) and DAPI (D1306, Thermo) or Hoechst (H3570, Thermo). To inhibit cytoskeleton components, before 1 hr for fixation, nocodazole (10 µM, M1404, Sigma), withaferin A (2 µM, 2816, Tocris), and latrunculin A (0.5 µM, 3973, Tocris) were individually treated 1 h before fixation and collected for further analysis.

Fluorescent images were acquired using inverted fluorescence microscopes (Olympus IX71, Tokyo, Japan; Nikon ECLIPSE Ti2, Minato City, Tokyo, Japan) with emission at 405, 488, 561, and 647 nm. Cell number, area, alignment, aspect ratio, and protein expression levels were analyzed using ImageJ software (version 1.53t, USA). The Nuclear Shape Index (NSI) was calculated from fluorescence staining images using the formula NSI = $4\pi A/p^2$, where $A$ denotes the nuclear area and $p$ represents the nuclear perimeter. Nuclear aspect ratio was calculated as the ratio of long axis to short axis from 2D projected nuclear images. Nuclear flattening was calculated as the ratio between the long axis length measured from 2D projected nuclear images and nuclear height (from 3D images). Confocal imaging was performed with a Nikon ECLIPSE Ti2 inverted microscope equipped with a Nikon C2+ confocal laser scanning system (Minato City, Tokyo, Japan). Images were processed and analyzed using either ImageJ or Nikon NIS-Elements AR software (version 5.24.01). Nikon's structured illumination microscopy (N-SIM) images were captured using Nikon (A1R HD25, NiKon, Minato City, Tokyo, Japan) microscope with an x60 objective with emission at 405 nm (Dapi) and 561 nm (AcH3). All fluorescence intensity values were normalized to the average values from control condition (Flat) and represented as relative values in graphs.

*Sequencing —Assay for Transposase-Accessible Chromatin with Sequencing (ATAC-seq)*: $6 \times 10^4$ rMSC were seeded onto large disc (Ø = 30 mm) and allowed to grow for 24 h before ATAC-seq. The cells were washed twice with ice-cold HBSS and collected with scrapper after adding lysis buffer on ice. Subsequently, cell lysates were centrifuged at 500 g for 10 min at 4 °C and the supernatant was removed. Tn5 Transposase (Cat #FC-121- 1030) was then added and incubated for 30 min at 37 °C, followed by DNA purification was proceeded (28004, MinElute PCR purification Kit, Qiagen).

Furthur process was followed by manufacturer's protocol.[25] Briefly, transposed DNA fragments were amplified using a PCR-based library preparation protocol (Nextera DNA Flex) optimized to minimize GC and size bias. Additional cycles were determined by qPCR to target 1/4 maximum fluorescence intensity. Final libraries were purified, quantified by KAPA qPCR and qualified on a Bioanalyzer (Agilent Technologies) per standard pipelines prior to Illumina HiSeq. Raw reads were analyzed (ExPADA, Ebiogen Inc., South Korea) to identify regions of significant chromatin accessibility.

*Sequencing —Total Cell RNA Sequencing*: MSCs were seeded at a density of $1 \times 10^4$ cells per disc on the specimen and incubated for 24 h under growth media and another 24 or 72 h under osteogenic media. Following the manufacturer's protocol, total mRNA was extracted from the cells using Ribospin II (GeneAll, South Korea). Next, mRNA transcripts were sequenced (Ebiogen Inc., South Korea) and data processed to quantify significantly differential expression (ExDEGA) using fold change criteria (>1.5 or 1.3). Public databases including DAVID (http://david.abcc.ncifcrf.gov) and Medline (http://www.ncbi.nlm.nih.gov) were used to annotate biological functions of gene sets. A core YAP signature was curated from published overexpressing models (MCF10A cells overexpressing YAP1).[26] Other transcriptional roles were literature-confirmed.

*Differentiation of MSCs and Mechanotransduction Analysis*: For osteogenesis experiments, 5000 rMSCs were seeded on Ø10 mm specimens in GM. The following day, the medium was replaced with osteogenic medium ($\alpha$-MEM supplemented with 10% FBS, 1% P/S, 50 µg $mL^{-1}$ ascorbic acid, 10 nM dexamethasone, and 10 mM $\beta$-glycerophosphate),[27] which was refreshed every 3 days. After 3 days of osteogenic differentiation, qRT-PCR was performed to analyze the gene expression levels of *RUNX2*, *Col1A*, *ALP*, *BSP*, *OCN*, *CREBBP (KAT3A)*, and *CTGF* according to the previous methodology.[21,28] The primer sequences used are listed in Table S5 (Supporting Information). For immunofluorescence analysis, Verteprfin (VP, 1 or 2 µM, 5305, Tocris) and C646 (10 µM, 4200, Tocris) were administered in osteogenic medium for 24 h. Due to cytotoxicity concerns, nocodazole was treated only for 1 h before fixation under osteogenic medium (24 h). Subsequently, the cells were stained with antibodies against Yap (1:50, Cell signaling), RUNX2 (1:50, abcam), and histone 3 acetylation (1:200). Quantification of fluorescence signals was performed using ImageJ software.

For maturation analysis, inhibitors were applied under osteogenic medium, with changes every 3 days. Exceptionally, Nocodazole was treated for 1 hr before each medium change during 9 days of differentiation. Each specimen was fixed with paraformaldehyde (4%) for 15 min at room temperature and subjected to Alizarin Red S solution at pH 4.2 for 30 min. Stained samples were observed using a digital camera, and quantification was performed by dye extraction. The stain was extracted using 10% (w/v) cetylpyridinium cholofide, and absorbance was measured at 562 nm with a spectrophotometer (Thermo). Details of the inhibitors schedule and concentrations are shown in Figure S35 and Table S6 (Supporting Information).

*Hemolysis Assay*: Blood compatibility was evaluated using hemolysis assay. Whole blood was collected from the hepatic vein of 15-week-old male Sprague–Dawley (SD) rats into K2EDTA-coated Microtainer tubes (BD Biosciences, Franklin Lakes, NJ, USA) to prevent coagulation. Red blood cells (RBCs) were isolated by centrifuging whole blood at 3000 rpm for 16 min. The cell pellet was washed three times with PBS (10 mL, 3000 rpm, 5 min each), and RBCs were resuspended in PBS at a final concentration of 5% (v/v). Flat and W-NT titanium disk samples (10 mm in diameter) were immersed in 600 µL of the 5% RBC suspension in 4-well plates and incubated at 37 °C for 4 h. PBS and 1% Triton X-100 were used as the negative and positive controls, respectively, under the same incubation conditions.

Following incubation, RBS suspensions were transferred to microcentrifuge tubes, and centrifuged at 3000 rpm for 10 min. The absorbance of the supernatant was measured at 540 nm using a microplate reader.

The hemolysis ratio (%) was calculated using the following equation:

$$\text{Hemolysis } (\%) = [(A_S - A_P) / (A_T - A_P)] \times 100 \quad (1)$$

where As, Ap and $A_T$ represent the absorbance values of the sample, PBS, and 1% Triton X-100 respectively.

*Implant Stability Test*: Implant stability test was performed using commercially available internal-type dental implants (TFS5008, Ø5.0 × 8 mm, KJmeditech Co., Ltd., Gwangju, Korea) with three different surface treatments: machined (Flat), FsL-derived nanostructured (W-NT, B2LAB Co., Ltd., Seoul, Korea), and sandblasted with large-grit and acid-etched (SLA). Artificial bone blocks of polyurethane foam (20 pcf, Sawbones, Washington, USA) mimicking D2-type alveolar bone were utilized as testing substrates. Three different surface fixtures were implanted in each block ($n$ = 5). Implant site preparation followed the manufacturer's protocol using the Osstem Taper Kit. An NSK Surgic XR Plus engine operating at 1200 rpm was employed for implant placement with an initial standardized torque of 30 N·cm, subsequently adjusted to achieve precise positioning with two threads visible above the bone surface. All surgical experiments were conducted by a dental implant specialist with over 15 years of experience. Primary stability was immediately assessed by resonance frequency analysis using Osstell IDx (Osstell AB, Gothenburg, Sweden), with measurements recorded as implant stability quotient (ISQ) values. The final adjusted insertion torque required to reach standardized depth was recorded from the surgical engine's digital display. For torque values exceeding 50 N·cm, a manual torque instrument was used and recorded as 55 N·cm for comparison. Pull-out strength testing was conducted using an Instron 3344 universal testing machine (Instron Corp., Norwood, MA, USA) at a constant crosshead speed of 10 mm $min^{-1}$ until complete implant displacement, with maximum load (N) recorded as the immediate retention ability.

*In Vivo Study—Mouse Tooth Model*: This study was approved by the Institutional Animal Care and Use Committee of Dankook University (Approval ID: DKU-24-061, Republic of Korea). Male C57BL/6 mice (3 weeks old, n = 3 per group) were anesthetized via intraperitoneal injection of ketamine (100 mg $kg^{-1}$) and xylazine (5 mg $kg^{-1}$). The left maxillary first molar (M1) was extracted, and the animals were monitored until the following day to ensure full recovery from anesthesia. The extraction sites were left to heal for 4 weeks to allow bone regeneration.

At 4 weeks post-extraction, titanium screw (Ti screw) implantation was performed. Mice were anesthetized as described above, and a surgical site was prepared using a drill machine (Strong 207b, China) with a Ø 0.75 mm drill bit operating at 10 000 RPM. Ti screws (laser-treated/untreated, $n = 3$, Ø 1 mm, height 1.42 mm, Table S7, Supporting Information) were carefully inserted into the drill site using a driver. Two weeks after implantation, the mice were euthanized by $CO_2$ asphyxiation, and the maxillary bones were harvested for analysis.

The Ti screws were gently removed, and the maxillary bone samples were fixed in 4% paraformaldehyde (PFA) for 48 h at 4 °C. The samples were decalcified in 10% EDTA (pH 7.4) in PBS for 14 days at 4 °C. After rinsing with PBS, the samples were dehydrated and embedded in paraffin using a 1:1 mixture of hard paraffin (1568, Duksan, Korea) and soft paraffin (39601006, Leica, USA). Paraffin-embedded samples were sectioned vertically along the implant axis at a thickness of 5 µm for immunohistochemical (IHC) analysis to examine AcH3, YAP, and $\alpha$-tubulin expression (Table S3, Supporting Information). IHC results were captured using confocal microscopy, and the intensity of AcH3, YAP, and $\alpha$-tubulin was measured in cells located in the single layer adjacent to the implant in each image using ImageJ software.

*In Vivo Study—Rabbit Tibia Model*: To evaluate osseointegration of green-processed topography, six New Zealand white rabbits (≈3.5 kg each) were used, with approval from the Institutional Animal Care and Use Committee (CRONEX-IACUC 202004002). Rabbits were provided food and distilled water ad libitum.

Two round defects were created in both the right and left tibiae of each rabbit. Three types of grade 4 Ti screws (laser-treated/untreated one and SLA from Dentium (Korea, Suwon), $n = 7$, Ø 3.4 mm, height 6 mm, Table S7, Supporting Information) were randomly positioned in the defects within the cortical bone with firm fixation. After 4 weeks of healing, the rabbits were sacrificed, and the samples were fixed in 10% neutral buffered formalin (NBF) solution.

The samples were scanned using µ-CT and analyzed with SkyScan software (Aartselaar, Belgium) under the following conditions: X-ray source at

385 µA and 65 kV, 9 µm section thickness, and 279 ms exposure time. 3D reconstruction and quantitative analysis of hard tissue generation were performed using 3D Slicer (Ver. 4.11.0), MeshLab (Ver. 2020.0), and Blender™ (Blender Foundation, Amsterdam, the Netherlands).

Histological analysis of the bone tissues was performed with H&E and Masson's trichrome (MT) staining. Inflammatory responses at the Ti-bone interface were assessed using a light microscope (BX50; Olympus, Tokyo, Japan). Histomorphometric analysis was conducted to calculate bone-to-implant contact (BIC) and bone area (BA) within the first two threads in the cortical bone. Measurements were performed individually for both left and right sides of the bone-screw interface using image analysis software (Image-Pro Plus, Media Cybernetics, Silver Spring, MD, USA; iMT i-Solution, Vancouver, Canada) (n = 14).

*In Vivo Study—Inflammation Scoring*: Biocompatibility of titanium implants was assessed by evaluating inflammatory responses at the implant-tissue interface according to ISO 10993-6:2016 Annex E guidelines.[29] Two animal models were employed: a mouse alveolar bone model with non-submerged implantation (Flat and W-NT surfaces, $n = 3$ per group, 2-week healing) and a rabbit tibia model with submerged implantation (Flat, W-NT, and SLA mini screws, $n = 3$ per group, 4-week healing). Following sacrifice, tissue samples were prepared for hematoxylin and eosin staining. All histological evaluations were performed by a professionally trained pathologist blinded to sample identities. Inflammatory responses were scored semi-quantitatively by evaluating the presence of inflammatory cells (x1, polymorphonuclear cells, lymphocytes, plasma cells, macrophages, giant cells) and tissue reactions (x2, necrosis, neovascularization, fibrosis, fatty infiltrate). Each parameter was scored from 0-4 (0: absent; 1: minimal; 2: mild; 3: moderate; 4: marked) according to ISO 10993-6:2016 Annex E guidelines. Mean scores were calculated and compared between groups using unpaired t-tests, with $p < 0.05$ considered statistically significant.

*Statistical Analysis*: All results are presented as the mean (or median) ± one standard deviation (SD) based on at least three independent experiments. Data normality was assessed using the Shapiro-Wilk test. Comparisons between two groups were conducted using a two-tailed Student's *t*-test. For multiple group comparisons, one-way analysis of variance (ANOVA) was performed, followed by Tukey's or Dunnett's post hoc test, depending on the experimental design. Pearson's correlation coefficient ($r$) with two-tailed $p$-values was calculated to evaluate relationships between variables, and scatter plots with fitted lines were generated for visual representation. A $p$-value of <0.05 was considered statistically significant, with significance levels indicated as follows: $p < 0.05$ (* or #), $p < 0.01$(**), $p < 0.001$ (***), and $p < 0.0001$ (****). Statistical analyses were conducted using GraphPad Prism software (version 9.5.1).

## Supporting Information

Supporting Information is available from the Wiley Online Library or from the author.

## Acknowledgements

This work was supported by grants from the National Research Foundation (RS-2024-00334160, RS-2024-00348908, 2021R1A5A2022318, RS-2023-00220408), Republic of Korea. This work was also supported by Ministry of Trade, Industry, and Energy (MOTIE), Republic of Korea, under the "Industrial Innovation Infrastructure Establishment Project" (reference number P0018140) supervised by the Korea Institute for Advancement of Technology (KIAT). Dr. Amal George Kurian helped to conduct the XPS analysis.

## Conflict of Interest

The authors declare no conflict of interest.

## Author Contributions

B.J. and J.-Y.Y. contributed equally to this work. B.J., J.-Y.Y., S.-H.L., H.H.L., H.-W.K., and J.-H.L. conceptualized the study and designed the experiments; B.J., B.B., J.C.K., J.-Y.Y., J.A., B.L., S.-M.P., D.L., Y.-J.K, S.L, M.-Y.L., and J.-H.K. performed experiments. B.J., J.-Y.Y., S.-H.L., H.H.L., H.-W.K., and J.-H.L. analyzed the data including statistics and prepared the first draft. S.-H.L., H.H.L., H.-W.K., and J.-H.L. provided funds for the study. All other coauthors reviewed and edited it. All authors read and approved the final draft and take full responsibility for its content, including the accuracy of the data and its statistical analysis.

## Data Availability Statement

The data that support the findings of this study are available from the corresponding author upon reasonable request.

## Keywords

eco-friendly, femtosecond laser, nanotopography, nuclear mechanosensing, osteogenesis

Received: February 6, 2025
Revised: June 4, 2025
Published online:

[1] a) C. S. Hansel, S. W. Crowder, S. Cooper, S. Gopal, M. João Pardelha da Cruz, L. de Oliveira Martins, D. Keller, S. Rothery, M. Becce, A. E. Cass, *ACS Nano* **2019**, *13*, 2913; b) H. Seong, S. G. Higgins, J. Penders, J. P. Armstrong, S. W. Crowder, A. C. Moore, J. E. Sero, M. Becce, M. M. Stevens, *ACS Nano* **2020**, *14*, 5371; c) J. T. Robinson, M. Jorgolli, A. K. Shalek, M.-H. Yoon, R. S. Gertner, H. Park, *Nat. Nanotechnol.* **2012**, *7*, 180; d) C. Chiappini, X. Liu, J. R. Fakhoury, M. Ferrari, *Adv. Funct. Mater.* **2010**, *20*, 2231; e) C. Xie, Z. Lin, L. Hanson, Y. Cui, B. Cui, *Nat. Nanotechnol.* **2012**, *7*, 185; f) X. Xie, A. M. Xu, S. Leal-Ortiz, Y. Cao, C. C. Garner, N. A. Melosh, *ACS Nano* **2013**, *7*, 4351.

[2] a) S. Dupont, L. Morsut, M. Aragona, E. Enzo, S. Giulitti, M. Cordenonsi, F. Zanconato, J. Le Digabel, M. Forcato, S. Bicciato, N. Elvassore, S. Piccolo, *Nature* **2011**, *474*, 179; b) E. D. Tabdanov, V. Puram, A. Zhovmer, P. P. Provenzano, *Cell Rep.* **2018**, *25*, 328; c) L. Lv, Y. Liu, P. Zhang, X. Zhang, J. Liu, T. Chen, P. Su, H. Li, Y. Zhou, *Biomaterials* **2015**, *39*, 193; d) R. S. Stowers, A. Shcherbina, J. Israeli, J. J. Gruber, J. Chang, S. Nam, A. Rabiee, M. N. Teruel, M. P. Snyder, A. Kundaje, O. Chaudhuri, *Nat. Biomed. Eng.* **2019**, *3*, 1009.

[3] a) S. Vermeulen, B. Van Puyvelde, L. Bengtsson del Barrio, R. Almey, B. K. van der Veer, D. Deforce, M. Dhaenens, J. de Boer, *Adv. Sci.* **2023**, *10*, 2203880; b) S.-H. Um, J. Lee, I.-S. Song, M.-R. Ok, Y.-C. Kim, H.-S. Han, S.-H. Rhee, H. Jeon, *Bioact. Mater.* **2021**, *6*, 3608; c) X. Wang, V. Agrawal, C. L. Dunton, Y. Liu, R. K. A. Virk, P. A. Patel, L. Carter, E. M. Pujadas, Y. Li, S. Jain, H. Wang, N. Ni, H.-M. Tsai, N. Rivera-Bolanos, J. Frederick, E. Roth, R. Bleher, C. Duan, P. Ntziachristos, T. C. He, R. R. Reid, B. Jiang, H. Subramanian, V. Backman, G. A. Ameer, *Nat. Biomed. Eng.* **2023**, *7*, 1514.

[4] a) J.-W. Choi, Y.-C. Kim, *Plast. Aesthetic Res.* **2023**, *10*, 59; b) L. Autelitano, M. C. Meazzini, *Plast. Aesthetic Res.* **2023**, *10*, 16; c) D. Khurana, A. Suresh, R. Nayak, M. Shetty, R. K. Sarda, J. C. Knowles, H.-W. Kim, R. K. Singh, B. N. Singh, *J. Tissue Eng.* **2024**, *15*, 20417314241228118; d) J. R. Schmidt, K. Adamowicz, L. Arend, J. Lehmann, M. List, P. S. Poh, J. Baumbach, S. Kalkhof, T. Laske, *J. Tissue Eng.* **2024**, *15*, 20417314241295332.

[5] a) O. Chaudhuri, J. Cooper-White, P. A. Janmey, D. J. Mooney, V. B. Shenoy, *Nature* **2020**, *584*, 535; b) A. J. Engler, S. Sen, H. L. Sweeney, D. E. Discher, *Cell* **2006**, *126*, 677; c) R. McBeath, D. M. Pirone, C. M. Nelson, K. Bhadriraju, C. S. Chen, *Dev. Cell* **2004**, *6*, 483; d) I. Cockerill, Y. Su, J. H. Lee, D. Berman, M. L. Young, Y. Zheng, D. Zhu, *Nano Lett.* **2020**, *20*, 4594; e) M. J. Dalby, N. Gadegaard, R. Tare, A. Andar, M. O. Riehle, P. Herzyk, C. D. W. Wilkinson, R. O. C. Oreffo, *Nat. Mater.* **2007**, *6*, 997; f) M. J. Dalby, A. J. García, M. Salmeron-Sanchez, *Nat. Rev. Mater.* **2018**, *3*, 17091; g) Y. Lei, Q. Zhang, G. Kuang, X. Wang, Q. Fan, F. Ye, *Smart Med.* **2022**, *1*, 20220014; h) Y. Xu, Q. Saiding, X. Zhou, J. Wang, W. Cui, X. Chen, *Smart Med.* **2024**, *3*, 20230034; i) H. Zhu, J. Wang, S. Wang, Y. Yang, M. Chen, Q. Luan, X. Liu, Z. Lin, J. Hu, K. Man, J. Zhang, *J. Tissue Eng.* **2024**, *15*, 20417314241244997; j) S. Azadi, M. A. Yazdanpanah, A. Afshari, N. Alahdad, S. Chegeni, A. Angaji, S. M. Rezayat, S. Tavakol, *J. Tissue Eng.* **2024**, *15*, 20417314241303818.

[6] a) B. J. McKenzie, R. Haas, G. E. Ferreira, C. G. Maher, R. Buchbinder, *PLoS One* **2022**, *17*, 0276685; b) A. Insua, P. Galindo-Moreno, R. J. Miron, H.-L. Wang, A. Monje, *Periodontology 2000* **2024**, *94*, 27; c) Y. Zhu, H. Liang, X. Liu, J. Wu, C. Yang, T. M. Wong, K. Y. H. Kwan, K. M. C. Cheung, S. Wu, K. W. K. Yeung, *Sci. Adv.* **2021**, *7*, abf6654.

[7] a) L. Bai, P. Chen, Y. Zhao, R. Hang, X. Yao, B. Tang, C. Liu, Y. Xiao, R. Hang, *Biomaterials* **2021**, *278*, 121162; b) P. A. Erturk, S. Altuntas, G. Irmak, F. Buyukserin, *J. Biomed. Mater. Res., Part A* **2025**, *113*, 37792; c) M. Ganjian, K. Modaresifar, D. Rompolas, L. E. Fratila-Apachitei, A. A. Zadpoor, *Acta Biomater.* **2022**, *140*, 717; d) R. A. Gittens, T. McLachlan, R. Olivares-Navarrete, Y. Cai, S. Berner, R. Tannenbaum, Z. Schwartz, K. H. Sandhage, B. D. Boyan, *Biomaterials* **2011**, *32*, 3395; e) V. K. Manivasagam, K. C. Popat, *Mater. Sci. Eng. C-Mater. Biol. Appl.* **2021**, *128*, 112315; f) S. Oh, K. S. Brammer, Y. S. Li, D. Teng, A. J. Engler, S. Chien, S. Jin, *Proc. Natl. Acad. Sci. USA* **2009**, *106*, 2130; g) C. R. Pedrosa, D. Arl, P. Grysan, I. Khan, S. Durrieu, S. Krishnamoorthy, M. C. Durrieu, *ACS Appl. Mater. Interfaces* **2019**, *11*, 8858; h) G. Zhu, S. Zou, R. Yao, Z. Ma, Y. Zhang, X. Zhao, G. Wang, *Mater. Lett.* **2022**, *313*, 131739.

[8] a) K. Sugioka, Y. Cheng, *Appl. Phys. Rev.* **2014**, 1; b) J. Ma, J. Wu, Z. Lin, J. Wang, W. Yao, Y. Zhang, X. Zhang, L. Zhu, Y. Hayasaki, H. Zhang, *Small Sci.* **2025**, *5*, 2400400; c) W. A. Lackington, P. Schweizer, M. Khokhlova, C. Cancellieri, S. Guimond, A.-L. Chopard-Lallier, J. Hofstetter, P. Schmutz, X. Maeder, M. Rottmar, *Adv. Mater. Interfaces* **2022**, *9*, 2201164; d) X. Pan, W. He, Z. Cai, X. Wang, P. Liu, S. Luo, L. Zhou, *Chin. J. Aeronaut.* **2022**, *35*, 521; e) Y. Liu, Z. Rui, W. Cheng, L. Song, Y. Xu, R. Li, X. Zhang, *Regen. Biomater.* **2021**, *8*, 521.

[9] A. Y. Vorobyev, C. Guo, *Laser Photonics Rev.* **2013**, *7*, 385.

[10] a) J. Pan, H. Li, K. Jin, H. Jiang, K. Li, Y. Tang, Z. Liu, K. Zhang, K. Chen, Z. Xu, H. Wang, H. Yang, J. Niu, Q. Shi, H. Chen, *Mater. Today Bio* **2023**, *18*, 100519; b) J. He, D. You, Q. Li, J. Wang, S. Ding, X. He, H. Zheng, Z. Ji, X. Wang, X. Ye, C. Liu, H. Kang, X. Xu, X. Xu, H. Wang, M. Yu, *Adv. Sci.* **2022**, *9*, 2200053; c) J. Zhang, J. Liu, C. Wang, F. Chen, X. Wang, K. Lin, *Bioact. Mater.* **2020**, *5*, 9; d) M. Zhu, H. Ye, J. Fang, C. Zhong, J. Yao, J. Park, X. Lu, F. Ren, *ACS Appl. Mater. Interfaces* **2019**, *11*, 43888; e) Y. Zhang, S. E. Chen, J. Shao, J. J. J. P. van den Beucken, *ACS Appl. Mater. Interfaces* **2018**, *10*, 36652; f) D. Karazisis, L. Rasmusson, S. Petronis, A. Palmquist, F. A. Shah, H. Agheli, L. Emanuelsson, A. Johansson, O. Omar, P. Thomsen, *Acta Biomater.* **2021**, *136*, 279; g) G.-Y. Zhu, Y.-H. Liu, W. Liu, X.-Q. Huang, B. Zhang, Z.-L. Zheng, X. Wei, J.-Z. Xu, Z.-H. Zhao, *ACS Omega* **2021**, *6*, 21792; h) K. Metavarayuth, P. Maturavongsadit, X. Chen, P. Sitasuwan, L. Lu, J. Su, Q. Wang, *Nano Lett.* **2019**, *19*, 8372; i) L. Li, S. Yang, L. Xu, Y. Li, Y. Fu, H. Zhang, J. Song, *Acta Biomater.* **2019**, *96*, 674; j) W. Qian, L. Gong, X. Cui, Z. Zhang, A. Bajpai, C. Liu, A. B. Castillo, J. C. M. Teo, W. Chen, *ACS Appl. Mater. Interfaces* **2017**, *9*, 41794; k) Q.-R. Xiao, N. Zhang, X. Wang, X.-Y. Man, K. Yang, L.-X. Lü, N.-P. Huang, *Adv. Mater. Interfaces* **2017**, *4*, 1600652.

[11] C. F. Holder, R. E. Schaak, *ACS Nano* **2019**, *13*, 7359.

[12] a) M. J. Dalby, N. Gadegaard, R. O. C. Oreffo, *Nat. Mater.* **2014**, *13*, 558; b) J.-H. Lee, D.-H. Kim, H.-H. Lee, H.-W. Kim, *Biomaterials* **2019**, *197*, 60; c) E. A. Ross, L.-A. Turner, H. Donnelly, A. Saeed, M. P. Tsimbouri, K. V. Burgess, G. Blackburn, V. Jayawarna, Y. Xiao, M. A. G. Oliva, J. Willis, J. Bansal, P. Reynolds, J. A. Wells, J. Mountford, M. Vassalli, N. Gadegaard, R. O. C. Oreffo, M. Salmeron-Sanchez, M. J. Dalby, *Nat. Commun.* **2023**, *14*, 753.

[13] a) O. Hamant, D. Inoue, D. Bouchez, J. Dumais, E. Mjolsness, *Nat. Commun.* **2019**, *10*, 2360; b) R. K. Singh, A. G. Kurian, V. Sagar, I. Park, J.-H. Park, H. Lee, J.-H. Lee, H.-W. Kim, *Adv. Funct. Mater.* **2023**, *33*, 2304821.

[14] a) S. Seetharaman, B. Vianay, V. Roca, A. J. Farrugia, C. De Pascalis, B. Boëda, F. Dingli, D. Loew, S. Vassilopoulos, A. Bershadsky, M. Théry, S. Etienne-Manneville, *Nat. Mater.* **2022**, *21*, 366; b) R. H. Abbassi, A. Recasens, D. C. Indurthi, T. G. Johns, B. W. Stringer, B. W. Day, L. Munoz, *ACS Pharmacol. Transl. Sci.* **2019**, *2*, 402.

[15] Y. Kalukula, A. D. Stephens, J. Lammerding, S. Gabriele, *Nat. Rev. Mol. Cell Biol.* **2022**, *23*, 583.

[16] a) Y. Qiao, R. Wang, X. Yang, K. Tang, N. Jing, *J. Biol. Chem.* **2015**, *290*, 2508; b) M. Völker-Albert, A. Bronkhorst, S. Holdenrieder, A. Imhof, *Stem Cell Rep.* **2020**, *15*, 1196.

[17] B. T. Sherman, M. Hao, J. Qiu, X. Jiao, M. W. Baseler, H. C. Lane, T. Imamichi, W. Chang, *Nucleic Acids Res.* **2022**, *50*, W216.

[18] M. Kanehisa, Y. Sato, *Protein Sci.* **2020**, *29*, 28.

[19] a) S. Moon, S. Lee, J. A. Caesar, S. Pruchenko, A. Leask, J. A. Knowles, J. Sinon, B. Chaqour, *iScience* **2020**, *23*, 101184; b) B. Zhao, X. Ye, J. Yu, L. Li, W. Li, S. Li, J. Yu, J. D. Lin, C.-Y. Wang, A. M. Chinnaiyan, Z.-C. Lai, K.-L. Guan, *Genes Dev.* **2008**, *22*, 1962; c) H. Luo, Q. Yu, Y. Liu, M. Tang, M. Liang, D. Zhang, T. S. Xiao, L. Wu, M. Tan, Y. Ruan, J. Bungert, J. Lu, *Sci. Adv.* **2020**, *6*, aaw4651; d) A. B. Keenan, D. Torre, A. Lachmann, A. K. Leong, M. L. Wojciechowicz, V. Utti, K. M. Jagodnik, E. Kropiwnicki, Z. Wang, A. Ma'ayan, *Nucleic Acids Res.* **2019**, *47*, W212.

[20] a) C. Yang, M. W. Tibbitt, L. Basta, K. S. Anseth, *Nat. Mater.* **2014**, *13*, 645; b) A. R. Killaars, C. J. Walker, K. S. Anseth, *Proc. Natl. Acad. Sci. USA* **2020**, *117*, 21258; c) M. Guo, A. F. Pegoraro, A. Mao, E. H. Zhou, P. R. Arany, Y. Han, D. T. Burnette, M. H. Jensen, K. E. Kasza, J. R. Moore, F. C. Mackintosh, J. J. Fredberg, D. J. Mooney, J. Lippincott-Schwartz, D. A. Weitz, *Proc. Natl. Acad. Sci. USA* **2017**, *114*, E8618.

[21] J.-Y. Yoon, N. Mandakhbayar, J. Hyun, D. S. Yoon, K. D. Patel, K. Kang, H.-S. Shim, H.-H. Lee, J.-H. Lee, K. W. Leong, H.-W. Kim, *Biomaterials* **2022**, *289*, 121792.

[22] a) N. Kittur, R. Oak, D. Dekate, S. Jadhav, P. Dhatrak, *Mater. Today: Proc.* **2021**, *43*, 1064; b) B. Al-Nawas, W. Wagner, K. A. Grötz, *Int. J. Oral Maxillofac. Implants* **2006**, *21*, 726.

[23] a) D. K. Owens, R. C. Wendt, *J. Appl. Polym. Sci.* **1969**, *13*, 1741; b) J.-H. Lee, J.-K. Jo, D.-A. Kim, K. D. Patel, H.-W. Kim, H.-H. Lee, *Dental Mater.* **2018**, *34*, 63.

[24] J.-J. Kim, A. El-Fiqi, H.-W. Kim, *ACS Appl. Mater. Interfaces* **2017**, *9*, 2059.

[25] R. K. Singh, A. G. Kurian, V. Sagar, I. Park, J.-H. Park, H. Lee, J.-H. Lee, H.-W. Kim, *Adv. Funct. Mater.* **2023**, *33*, 2304821.

[26] a) M. Cordenonsi, F. Zanconato, L. Azzolin, M. Forcato, A. Rosato, C. Frasson, M. Inui, M. Montagner, Anna R. Parenti, A. Poletti, Maria G. Daidone, S. Dupont, G. Basso, S. Bicciato, S. Piccolo, *Cell* **2011**, *147*, 759; b) J. Zhang, G. A. Smolen, D. A. Haber, *Cancer Res.* **2008**, *68*, 2789.

[27] A. G. Kurian, N. Mandakhbayar, R. K. Singh, J.-H. Lee, G. Jin, H.-W. Kim, *Mater. Today Bio.* **2023**, *20*, 100664.

[28] I.-S. Park, C. Mahapatra, J. S. Park, K. Dashnyam, J.-W. Kim, J. C. Ahn, P.-S. Chung, D. S. Yoon, N. Mandakhbayar, R. K. Singh, J.-H. Lee, K. W. Leong, H.-W. Kim, *Biomaterials* **2020**, *242*, 119919.

[29] a) ISO 10993-6:2016 Biological evaluation of medical devices Part 6: Tests for local effects after implantation, International Organization for Standardization; b) A. Dasgupta, N. Sori, S. Petrova, Y. Maghdouri-White, N. Thayer, N. Kemper, S. Polk, D. Leathers, K. Coughenour, J. Dascoli, R. Palikonda, C. Donahue, A. A. Bulysheva, M. P. Francis, *Acta Biomater.* **2021**, *128*, 186.